

AD-A237 885



RL-TR-91-83
Final Technical Report
June 1991



2

**THEORETICAL, EXPERIMENTAL AND
NUMERICAL STUDIES ON HYBRID
ACOUSTOOPTIC BISTABLE DEVICES**

Syracuse University

Dr. Partha P. Banerjee

DTIC
SELECTE
JUL 10 1991
S B D

APPROVED FOR PUBLIC RELEASE; DISTRIBUTION UNLIMITED.

91-04251



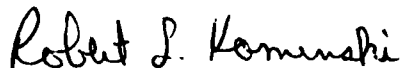
Rome Laboratory
Air Force Systems Command
Griffiss Air Force Base, NY 13441-5700

91 04251 2

This report has been reviewed by the Rome Laboratory Public Affairs Office (PA) and is releasable to the National Technical Information Service (NTIS). At NTIS it will be releasable to the general public, including foreign nations.

RL-TR-91-83 has been reviewed and is approved for publication.

APPROVED:



ROBERT L. KAMINSKI
Project Engineer

APPROVED:



RAYMOND P. URTZ, JR.
Technical Director
Directorate of Command & Control

FOR THE COMMANDER:



BILLY G. OAKS
Directorate of Plans & Programs

If your address has changed or if you wish to be removed from the Rome Laboratory mailing list, or if the addressee is no longer employed by your organization, please notify RL (COTC) Griffiss AFB, NY 13441-5700. This will assist us in maintaining a current mailing list.

Do not return copies of this report unless contractual obligations or notices on a specific document require that it be returned.

REPORT DOCUMENTATION PAGE

Form Approved
OMB No. 0704-0188

Public reporting burden for this collection of information is estimated to average 1 hour per response, including the time for reviewing instructions, searching existing data sources, gathering and maintaining the data needed, and completing and reviewing the collection of information. Send comments regarding this burden estimate or any other aspect of this collection of information, including suggestions for reducing this burden, to Washington Headquarters Services, Directorate for Information Operations and Reports, 1215 Jefferson Davis Highway, Suite 1204, Arlington, VA 22202-4302, and to the Office of Management and Budget, Paperwork Reduction Project (0704-0188), Washington, DC 20503.

1. AGENCY USE ONLY (Leave Blank)		2. REPORT DATE June 1991	3. REPORT TYPE AND DATES COVERED Final Jun 88 - Dec 88	
4. TITLE AND SUBTITLE THEORETICAL, EXPERIMENTAL AND NUMERICAL STUDIES ON HYBRID ACOUSTOOPTIC BISTABLE DEVICES			5. FUNDING NUMBERS C - F30602-88-D-0027 Task B-8-3562 PE - 63728F PR - 2529 TA - 01 WU - PC	
6. AUTHOR(S) Dr. Partha P. Banerjee				
7. PERFORMING ORGANIZATION NAME(S) AND ADDRESS(ES) Syracuse University Dept. of Electrical & Computer Engineering Syracuse NY 13244-1240			8. PERFORMING ORGANIZATION REPORT NUMBER N/A	
9. SPONSORING/MONITORING AGENCY NAME(S) AND ADDRESS(ES) Rome Laboratory (COTC) Griffiss AFB NY 13441-5700			10. SPONSORING/MONITORING AGENCY REPORT NUMBER RL-TR-91-83	
11. SUPPLEMENTARY NOTES Rome Laboratory Project Engineer: Robert L. Kaminski/COTC/(315) 330-2925				
12a. DISTRIBUTION/AVAILABILITY STATEMENT Approved for public release; distribution unlimited.			12b. DISTRIBUTION CODE	
13. ABSTRACT (Maximum 200 words) This final report provides a short summary of various bistable optical devices, with emphasis on the acoustooptic bistable device. Difference equations describing an acoustooptic system have been defined along with numerical simulations to study the system dynamics. A summary of experimental work performed to verify some of the effects of hysteresis and bistability is included. A study of some of the characteristics of the underlying dynamical system using conventional methods is also included. This report also gives an alternative explanation of hysteresis and indicates how to study the behavior of the system for time-varying inputs.				
14. SUBJECT TERMS Optical Bistable Devices, Acoustooptics, Digital Optical Computing			15. NUMBER OF PAGES 76	
			16. PRICE CODE	
17. SECURITY CLASSIFICATION OF REPORT UNCLASSIFIED	18. SECURITY CLASSIFICATION OF THIS PAGE UNCLASSIFIED	19. SECURITY CLASSIFICATION OF ABSTRACT UNCLASSIFIED	20. LIMITATION OF ABSTRACT U	

1. INTRODUCTION

Optical bistability refers to the existence of two stable states of an optical system for a given set of input conditions. It is interesting physically because it represents a new kind of nonlinear system in optics.

The typical characteristics of an optically bistable system are illustrated in Fig. 1. A gradual increase in input power produces a steady increase in the output power or intensity until reaching a critical value where the output jumps up. On decreasing the input, the output does not immediately fall sharply but remains on the upper branch of the curve until the input is reduced to a lower critical value, at which the output jumps down again. In the region between these two critical points, there are two stable states for a given incident power. In addition to being hysteretic, the system also shows switching transitions, usually at both edges of the bistable region. Also, the state the bistable device actually assumes depends on the direction in which it traverses the hysteretic curve, i.e., it has memory.

Now, the diffraction of light by sound has traditionally received a lot of attention not only because of its physical finesse, but also because of its effectiveness in modulating a light beam with an electrical signal, and its versatility in applications of image and signal processing. For a general understanding of the basic principles of acousto-optics, the reader is referred to Appendix A, which was developed in conjunction with the main investigation reported in this writeup.

For about a decade, however, researchers have been investigating other innovative applications of acousto-optics, one of them being the hybrid acousto-optic (AO) device. Essentially, this is the conventional AO



Dist	Availability Codes
A-1	Avail and/or Special

device but with a positive feedback incorporated in it. This rather fascinating application came at a time when engineers and physicists began to be interested in bistable optical devices in general, namely the nonlinear Fabri-Perot etalon, the linear/nonlinear interface and multiple quantum well semiconductor devices.

In what follows, I will first present a short summary of the various bistable devices mentioned above, with emphasis on the AO bistable device. In Section 3, the difference equations describing the AO system will be defined along with numerical simulations to study the system dynamics. Section 4 will contain a summary of the experimental work done by us to verify some of the effects of hysteresis and bistability. In Section 5, we will study some of the characteristics of the underlying dynamical system using conventional methods, give an alternative explanation of hysteresis and indicate how to study the behavior of the system for time-varying inputs.

2. OPTICAL BISTABILITY AND CHAOS

Optical bistability is a field of ever-growing interest because of its potential applications to all-optical logic requiring a threshold device. In fact, a large amount of work has been done in the design of architectures performing a variety of arithmetic functions in an all-optical environment (see, for instance, ref. [1]). The first observation of optical bistability was in sodium vapor [2]. Since then, bistability has been observed in different materials and in several types of configurations. Notable amongst this is the work done in connection with absorptive and dispersive optical bistability in a nonlinear Fabri-Perot

etalon (for an excellent analysis, see ref. [3]). While the first effect is observed when the operating frequency is close to the resonant frequency of the atoms constituting the Fabri- Perot, dispersive bistability is noticeable for large frequency detuning in a medium having a Kerr-type nonlinearity. Optical bistability has also been observed in nonlinear interference filters made from semiconductors using the nonlinearities of a ZnS intermediate layer [4]. Theories have been advanced on bistability and hysteretic behavior of the transmission and reflection coefficients during optical transmission across a linear/nonlinear interface, both for grazing incidence [5,6] and for normal incidence if the nonlinear medium is dispersive as well [7]. Observations of optical bistability have also been reported in multiple quantum well structures consisting of thin alternating layers of GaAs and $\text{Ga}_x\text{Al}_{1-x}\text{As}$ [8]. Other novel bistable devices include one based on beam self-trapping which eliminates the commonly used optical cavity, thus removing cavity build-up and decay time constants, and relaxing the bandwidth requirements on the laser [9].

The phenomenon of AO bistability and hysteresis forms a sub-class of such effects observed in hybrid optical devices. Notable amongst these is an electro-optic modulator with external feedback [10]. Feedback, whether extrinsic or intrinsic, is essential to bistability; in a hybrid device, it is an external electrical signal. Any optical phenomenon that leads to an output signal that is a nonlinear function of a parameter will exhibit bistability in the presence of a positive feedback. The AO bistable device works on a similar principle, and is shown in Fig. 2. If the diffracted light from an AO device operating in the Bragg or near- Bragg regime (see Fig. 2a) is detected by a photodetector, amplified and fed

back to the transducer driving the AO device in unison with the external electrical input, a bistable device results (see Fig. 2b). In Fig. 2, Ψ_{inc} , Ψ_0 and Ψ_1 denote the incident, zeroth order and first order electric fields; ϕ_B is the Bragg angle defined as

$$\phi_B \approx K/2k_0 \quad (2.1)$$

where K , k_0 denote the propagation constants of the sound and light respectively in the AO cell, and $\hat{\alpha}$ is indicative of the sound pressure through the cell, with $\hat{\alpha}_0$ being proportional to the external electrical input. β denotes the gain constant of the feedback amplifier. A block-diagrammatic representation of the experimental setup is discussed later in Sec. 4.

From a historical perspective along our lines of interest, one of the first contributions in the area was the demonstration of AO bistability and the design of an optically-controlled two-channel switch by Chrostowski and Delisle [11]. Self-pulsing and chaos in AO devices, both bulk and integrated, was later investigated by Chrostowski et al [12] and Jerominek et al [13] respectively. Optical multistability and oscillations in hybrid optical bistable systems in the presence of a delayed feedback was analyzed by Martin-Pereda and Muriel [14]. The onset of period-doubling bifurcations leading to chaos was also explained by Hopf et al [15] and Derstine et al [16] for a hybrid bistable system in the regime where the delay time of the feedback signal is much larger than the response time of the device. Concurrent with the work on hybrid bistable systems, there have been an enormous amount of research on chaos in optically bistable systems in general, and on the nature of dynamical

systems that can predict chaos. Examples to quote for the former are, for instance, observation of chaos in laser systems [17,18] and their analysis [19]. As for the latter, work mainly started out in the analysis of the quadratic map (an excellent reference is the book by Devaney [20]), and was generalized to other dynamical systems (see, for instance, Grebogi et al [21] and references therein). Periodic maps, which are pertinent to our case, having what is called a "topological degree" 0, as well as other maps having a topological degree 1, have been also studied [22,23], although approximations to the periodic function have sometimes been made. The same is true in the analysis of chaos in AO bistability [12], where a \sin^2 map has been approximated by a quadratic map.

3. DIFFERENCE EQUATIONS AND NUMERICAL SIMULATION

Referring to Fig. 2a, the interaction process between light and sound for ideal Bragg interaction may be described in terms of the coupled set of ODEs

$$\begin{aligned} d\psi_0/d\xi &= -j(\hat{\alpha}/2)\psi_1, \\ d\psi_1/d\xi &= j(\hat{\alpha}/2)\psi_0, \end{aligned} \tag{3.1}$$

where ξ ($\hat{=}z/L$) is a normalized distance in the direction of propagation of the light and $\hat{\alpha}$ is the peak phase delay encountered by the light in the AO interaction region [24]. The amplitude of the light at $z=1$ ($\xi=1$) is then given by

$$\Psi_1 = -j\Psi_{inc} \sin(\hat{\alpha}/2), \quad (3.2)$$

where the assumption made is that the sound pressure ($\propto \hat{\alpha}$) remains constant during the interaction. If, now, the first-order light is detected by a photodetector and the resulting electrical signal amplified and fed back in unison with the external bias $\hat{\alpha}_0$ (Fig. 2b), the effective $\hat{\alpha}$ scattering the light may be written as

$$\hat{\alpha} = \hat{\alpha}_0 + \tilde{\beta}|\Psi_1|^2 \quad (3.3)$$

where $\tilde{\beta}$ is the product of the gain constant β of the amplifier and the conversion efficiency of the photodetector.

Under the feedback action, note that $\hat{\alpha}$ can only be treated as a constant if the interaction time, given as the ratio of the laser beam width and the bulk speed of sound in the AO modulator, is much less than the delays incorporated by the finite response time of the photodetector, the RF sound cell driver and the feedback amplifier, or any other delay that may have been purposely installed (e.g., an optical fiber or a coaxial cable) in the feedback path. We will consider this case only. Corresponding to a fixed input ($\propto \hat{\alpha}_0$), this means that the output Ψ_1 (or $|\Psi_1|^2$) will undergo a series of iterations at every instant $\hat{\alpha}$ is updated through feedback action. The value of $|\Psi_1|^2 \triangleq y$ after n iterations may then be written as

$$y_{n+1} = \sin^2[(\hat{\alpha}_0 + \tilde{\beta}y_n)/2], \quad (3.4)$$

where we have assumed $\Psi_{inc} = 1$ for convenience.

The steady-state behavior of (3.4) ($n \rightarrow \infty$) is governed by the relation

$$y = \sin^2[(\hat{\alpha}_0 + \tilde{\beta}y)/2], \quad (3.5)$$

and is plotted in Fig. 3 for different values of $\tilde{\beta}$. Note that there exists a minimum value of $\tilde{\beta}$ for the steady-state curve to acquire an S-shape when plotted as a function of $\hat{\alpha}_0$. This can be readily found by differentiating (3.5) w.r.t. $\hat{\alpha}_0$ and setting the derivative to infinity. It may easily be shown that

$$\tilde{\beta} > 2 \quad (3.6)$$

for the steady-state curve to assume infinite gradients. That this corresponds to the onset of hysteresis may be shown either from the rigorous theory of dynamical systems (see Sec. 5) or by simple numerical simulation of (3.4) suitably modified to increase $\hat{\alpha}_0$ in infinitesimal steps of $\Delta\hat{\alpha}$:

$$y_{n+1} = \sin^2[((n+1)\Delta\hat{\alpha} + \tilde{\beta}y_n)/2]. \quad (3.7)$$

This is shown in Figs. 4a,b for $\tilde{\beta} = 2.3$ and 2.9 respectively. Note that the accuracy of the simulations critically depends on $\Delta\hat{\alpha}$. The area under the hysteresis curve also increases with increasing $\tilde{\beta}$, with a reduction in the values of both the upper and lower thresholds, defined in terms of $\hat{\alpha}_0$. We remark also that technically speaking, (2.4) denotes an autonomous dynamical system while (2.7) is an example of a nonautonomous dynamical system. However, inferences about nonautonomous dynamical systems can be

made from the autonomous models, to be shown later.

For $\tilde{\beta} > 3.0$, the plot of y_n vs. n (according to (3.7)) clearly shows, in addition to hysteresis, controlled oscillations which, as will be seen later, are due to period-doubling bifurcations (see Fig. 5). Also, the onset of oscillations depends on the value of $\Delta\hat{\alpha}$. Fig. 6 shows a plot of $\tilde{\beta}$ vs. $\hat{\alpha}_0$ for different values of $\Delta\hat{\alpha}$, from where the oscillations commence [26].

For those familiar with circuit theory, the equivalent circuit of the bistable device in terms of an electronic Schmitt trigger is shown in Fig. 7. It is easy to recognize that the transfer characteristic of the Schmitt trigger exhibits bistability and hysteresis when the loop gain is greater than 1. The differential gain of the AO bistable device may be defined as $\Delta y/\Delta\hat{\alpha}$ and may be calculated to be

$$\Delta y/\Delta\hat{\alpha} = (1/2)\sin \hat{\alpha} / [1 - (1/2)\tilde{\beta}\sin \hat{\alpha}] \stackrel{\Delta}{=} A/[1 - A\tilde{\beta}]. \quad (3.8)$$

In terms of circuit analysis, (3.8) denotes a system with positive feedback, and the system becomes unstable for $A\tilde{\beta} > 1$.

We comment, at this point, that in a practical AO system operating in the so-called "near-Bragg" regime, the interaction between light and sound occurs in a fashion more complicated than the model set forward in eq.(3.1). For instance, there are other diffracted orders present at the output of the AO cell even at Bragg incidence, due to the finite Q of the cell. The Q parameter is defined as

$$Q = 2\pi\lambda_0 L/\Lambda^2 \quad (3.9)$$

where λ_0 and Λ are the wavelengths of light and sound in the AO cell and L is the width of the AO cell. Typical values of Q range from 5 to 20 in near Bragg operation. The general interaction equations may be written as

$$d\psi_n/d\xi = -j(\hat{\alpha}/2) [\exp \{-j(Q\xi/2) [(\phi_{inc}/\phi_B) + (2n-1)]\} \psi_{n-1} + \exp\{j(Q\xi/2) [(\phi_{inc}/\phi_B) + (2n+1)]\} \psi_{n+1}]. \quad (3.10)$$

where ϕ_{inc} is the incident angle; ϕ_B is the Bragg angle (see 2.1) and the ψ_n 's refer to the various diffracted orders.

The steady-state behavior of such a system with positive feedback is given by the simultaneous solution of (3.10) [with proper boundary conditions] and (3.3). Note, however, that (3.10) is an infinite set of coupled differential equations. We restrict ourselves to four diffracted orders, e.g., $-1 \leq n \leq 2$ and assume $\phi_{inc} = -\phi_B$. Fig. 8 shows, for instance, the numerically computed hysteresis curves for the first order light by changing $\tilde{\beta}$ and with $Q = 20$. Notice that hysteresis starts when $\tilde{\beta} > 2$, as predicted from (3.6). With increasing $\tilde{\beta}$, the area under hysteresis loop increases.

We remark that hysteretic behavior is also observed numerically if the second order light ($n=2$) is detected instead. More on this will follow in the next Section.

4. EXPERIMENTAL OBSERVATIONS

Fig. 9a shows a detailed setup of the hybrid AO bistable device. The diffracted light is detected by the photodetector of the feedback circuit.

The feedback comprises a photodetector (see Fig. 9b) and a variable scaling adder (see Fig. 9c). In order to show the hysteretic behavior of the system, a unipolar sawtooth signal with a peak-to-peak voltage of 5 volts at a typical frequency of 1 kHz is injected into the scaling adder after the input buffer stage. This adds in phase with the detected signal from the photodetector and, as shown in Fig. 9a, modulates the 40 Mhz signal of the frequency generator which, in turn, drives the transducer in the AO cell. We may mention that after the detector circuit, a high-pass filter is employed to block any spurious DC voltage and noise signals (see Fig. 9b). The DC blocking is required since it otherwise impedes the useful gain of the feedback signal in the OP AMP amplifier.

For an operating frequency of 40 Mhz for the sound, the effective Q of the cell, which is a figure of merit for defining the operating regime of the AO device [24], works out to about 20, which signifies the so-called near-Bragg regime. This means that, strictly speaking, higher order diffraction would occur. Figs. 10a-c show the detected output V_D from the first order and the modulation on $\hat{\alpha}_0$ as a function of time, with the corresponding hysteresis curves V_D vs. $\hat{\alpha}_0$ for increasing values of the feedback parameter β , which was varied by changing the amplifier gain. For low values of β , there is no hysteresis as predicted from the Lissajous figure in Fig. 10a. A slight wrapping (or figure of eight) was observed in the Lissajous pattern because of distortion in the output owing to finite-amplitude inputs. As β increases, hysteresis develops, resulting in clipping of the output. The exact points denoting transitions in the output (see Fig. 10c) are determined by the threshold values on the corresponding hysteresis plots. Notice the asymmetry in the output with respect to the input due to the upper and lower thresholds of

hysteresis. Fig. 11 shows a plot of the width of the hysteresis curves, measured as the maximum between the up and down transitions, as a function of the feedback parameter β . Results depict a linear region in which the device could be operated as a programmable thresholding device.

Fig. 12 shows the hysteretic behavior if the second-order diffracted light were detected and fed back instead of the first order. A theoretical discussion of the effect starting from the multiple plane-wave formalism has been presented in the previous Section. We also monitored the width of the hysteresis curve as a function of β for this case. Results, plotted in Fig. 13, show an improvement over the first-order case (see Fig. 11) by an approximate factor of 2, leading us to speculate that the second-order operation may be more advantageous than first-order operation for certain applications.

At the moment, we are limited to values of $\hat{\alpha}_0$ for which we cannot observe the oscillations mentioned in the previous Section, because of limitations on the maximum RF output from our signal generator.

5. DYNAMICS OF AUTONOMOUS SYSTEM AND EXPLANATION OF HYSTERESIS

In this Section, we will first briefly describe some of the results from the theory of autonomous dynamical systems with special reference to eq. (3.4) which describes the AO system with feedback but for a fixed input $\hat{\alpha}_0$. We will then present an alternative explanation of hysteresis, and indicate how to study the response of the system to time-varying inputs.

5.1 The Autonomous System

From (3.4) and with the definitions

$$B = \tilde{\beta}/2\pi, \quad \phi = \tilde{\alpha}_0/2\pi, \quad u_{n+1} = (\tilde{\beta}/2\pi)y_{n+1}, \quad (5.1)$$

we get

$$u_{n+1} = B \sin^2 \pi(\phi + u_n) \stackrel{\Delta}{=} f(u_n) \quad (5.2)$$

where B and ϕ are parameters. Technically speaking, (5.2) is an example of a periodic map of topological degree 0 [22, 23].

A point u^* is a **fixed point** of $f(u)$ if $f(u^*) = u^*$. Furthermore, u^* is a **fixed point of period m** if $f^{(m)}(u^*) = u^*$, where $f^{(m)}(u)$ denotes the m -th. iterate of u under the map $f(\cdot)$

$$f^{(m)}(x) = f \circ \dots \circ f(x), \quad f \circ g(x) \stackrel{\Delta}{=} f(g(x)). \quad (5.3)$$

The periodic fixed point u^* of period m is **stable** if $|[f^{(m)}]'(u^*)| < 1$ [20]. The periodicity and the stability of the fixed points may be conveniently studied graphically as follows. Fig. 14 shows plots of f , $f(2)$, $f(4)$ and $f(100)$ over $[0,1]$ with $B=0.6$ and $\phi=0.6$. The horizontal axis is indicative of the initial conditions u_0 . It is clear that A is the unstable fixed point of f , and A , B and C are the unstable fixed points of $f(2)$. The points A through G are the fixed points of $f(4)$, of which D through G are stable. Thus, $f^{(n)}(u_0)$, $0 \leq u_0 \leq 1$, will tend to either of these four points as n gets larger, as shown by the plot of $f(100)$. The

points D through G are stable fixed points of period 4.

The dynamics of (5.2) also depends critically on ϕ . Fig. 15 shows plots of f , $f^{(2)}$, $f^{(4)}$ and $f^{(100)}$ over $[0,1]$ with $B=0.6$ and $\phi=0.7$. Note that while once again there are four stable fixed points of period 4, their values are considerably different from the previous case.

In general, the periodicity of the fixed points may increase as B increases. For instance, for the map (5.2) with $B=0.4$ and $\phi=0.2$, there is one stable fixed point and $f^{(n)}(x_0)$ tends to this value as $n \rightarrow \infty$ for all x_0 . The same map for $B=0.5$ and $\phi=0.2$ has one unstable fixed point for f and $f^{(2)}$, and two stable fixed points for $f^{(2)}$. Thus $f^{(n)}(x_0)$ for this case tends to either of these values as $n \rightarrow \infty$. Thus, the case $B=0.4$ has a fixed point of period 1, while $B=0.5$ has stable fixed points of period 2 for $\phi=0.2$. We remark that for $B=0.5$ and $\phi=0.1$, f has only one stable fixed point.

For large n , the trajectory of a certain initial condition may be readily tracked on the basis of the knowledge of the fixed points and the graph of f . For instance, it can be easily shown that an initial condition in the range BE (see Fig. 14), for instance, will assume the values corresponding to the coordinates of F, D, G and E for $n = 101, 102, 103$ and 104 respectively. For $n = 105 - 108$, the process will recur, and so on.

5.2 Explanation of Hysteresis

The dynamics of the autonomous map as in (5.2) may be used to explain hysteresis and bistability. As shown in Fig. 16, the curve $B \sin^2(\pi u)$ has been sketched along with various straight lines at an angle of 45° to the

horizontal axis. Given a certain value of $\phi (\propto \hat{\alpha}_0)$ in (5.2) corresponding to a particular input, it is clear that the fixed point can be determined either by shifting the $\sin^2(\pi u)$ curve to the left and finding its intersection with the straight line at 45° passing through the origin, or, alternately, by appropriately shifting the 45° line to the right. Note that a certain initial condition, e.g., $u_0 = 0$, will settle at the lower stable fixed point marked A since it is to the left of the unstable fixed point X. This will continue till $\hat{\alpha}_0$ (and hence ϕ) is large enough such that there is only one stable fixed point marked B. This defines the upper threshold and establishes a new fixed point. When $\hat{\alpha}$ is slowly reduced, the output y will be at the point marked C since the new initial value is to the right of X. This will continue till $\hat{\alpha}_0$ is low enough so that there is, once again, one stable fixed point marked D. This defines the lower threshold and the hysteresis is complete.

5.3 Analysis of Time-varying Inputs

In the simplest case, assume that the input [$\hat{\alpha}$ or ϕ] is not longer a constant but a square wave of a certain duty cycle. This case may be studied on the basis of the maps for $\phi = \phi_1$ and $\phi = \phi_2$ where $\phi_{1,2}$ are the two levels of the square wave. The procedure involves drawing the maps (similar to Figs. 14, 15) for each ϕ and then finding the "composition" of the two maps. The result of this composition indicates the nature of the fixed points, which, in turn, provides evidence of the behavior of the system when a square wave is applied as the input.

6. CONCLUSION

In this report, I have tried to summarize some of the aspects of AO bistability and chaos, putting things in perspective of other advances in the area of nonlinear optical bistable devices in general. Some of the experimental, numerical and theoretical work done by us in the area have been summarized, along with appropriate references to the work of others and existing theories. I hope that this overview serves as a starting point for the interested researcher, and as a summary for the experts.

Acknowledgment

This work was partially funded by the Rome Air Development Center, Rome, N.Y. The principal investigator would like to thank Drs. H. Kaplan and U. Banerjee of Syracuse University and Dr. T-C Poon of Virginia Tech. for helpful discussions.

REFERENCES

1. P.P. Banerjee and A. Ghafoor, *Appl. Opt.* 27, 4766, 1988.
2. S.L. McCall, H.M. Gibbs, G.G. Churchill and T.N.C. Venkatesan, *Bull. Am. Phys. Soc.* 20, 636, 1975.
3. L.A. Lugiato in *Progress in Optics* vol. XX1, E. Wolf ed. North-Holland: Amsterdam, 1984.
4. F.V. Karpushko and G.V. Sinitsyn, *Sov. J. Quant. Electron.* 9, 520, 1979.
5. A.E. Kaplan in *Optical Bistability*. C.M. Bowden, M. Ciftan and H.R. Robl eds. Plenum: New York, 1981.
6. W.J. Tomlinson, J.P. Gordon, P.W. Smith and A.E. Kaplan, *Appl. Opt.* 21, 2041, 1982.
7. G.Cao and P.P. Banerjee, *J. Opt. Soc. Amer. B* 6, 191, 1989.
8. H.M. Gibbs, S.S. Tarng, J.L. Jewell, D.A. Weinberger, K. Tai, A.C. Gossard, S.L. McCall, A. Passner and W. Wiegmann, *Appl. Phys. Lett.* 41, 221, 1982.
9. J.E. Bjorkholm, P.W. Smith, W.J. Tomlinson and A.E. Kaplan, *Opt. Lett.* 6, 345, 1982.
10. E. Garmire, J.H. Marburger and S.D. Allen, *Appl. Phys. Lett.* 32, 320, 1978.
11. J. Chrostowski and C. Delisle, *Opt. Comm.* 41, 71, 1982.
12. J. Chrostowski, R. Vallee and C. Delisle, *Can. J. Phys.* 61, 1143, 1983.
13. H. Jerominek, C. Delisle, J.Y.D. Pomerleau and R. Tremblay, *Can. J. Phys.* 63, 227, 1985.
14. J.A. Martin-Pereda and M.A. Muriel, in *Optical Bistability 2*. Plenum: New York, 1984.
15. F.A. Hopf, D.L. Kaplan, H.M. Gibbs and R.L. Shoemaker, *Phys. Rev. A* 25, 2172, 1982.
16. M.W. Derstine, H.M. Gibbs, F.A. Hopf and D.L. Kaplan, *Phys. Rev. A* 27, 3200, 1983.
17. F.T. Arecchi, R. Meucci, G.P. Puccioni and J. R. Treicce, *Phys. Rev. Lett.* 49, 1217, 1982.
18. R.S. Gioggia and N.B. Abraham, *Phys. Rev. Lett.* 51, 650, 1983.
19. H.G. Solari, E. Eschenaji, R. Gilmore and J.R. Tredecce, *Opt. Comm.* 64, 49, 1987.
20. R.L. Devaney, *An Introduction to Chaotic Dynamical Systems*. Benjamin-Cummings: Menlo Park, California, 1986.
21. C. Grebogi, E. Ott and J. Yorke, *Science* 238, 632, 1987.
22. N. Ikeda, H. Tsuruta and T. Sato, *Biol. Cybern.* 42, 117, 1981.
23. J. Belair and L. Glass, *Phys. Lett.* 96A, 113, 1983.
24. A. Korpel, *Acousto-Optics*. Marcel Dekker: New York, 1988.
25. T-C Poon and S.K. Cheng, "Performance of Hybrid Bistable Devices using an Acousto-Optic modulator" to appear in *Appl. Opt.*
26. P.P. Banerjee and T-C Poon, *Proc. 30th. Midwest Sym. in Circuits and Systems*, North-Holland, 1987.

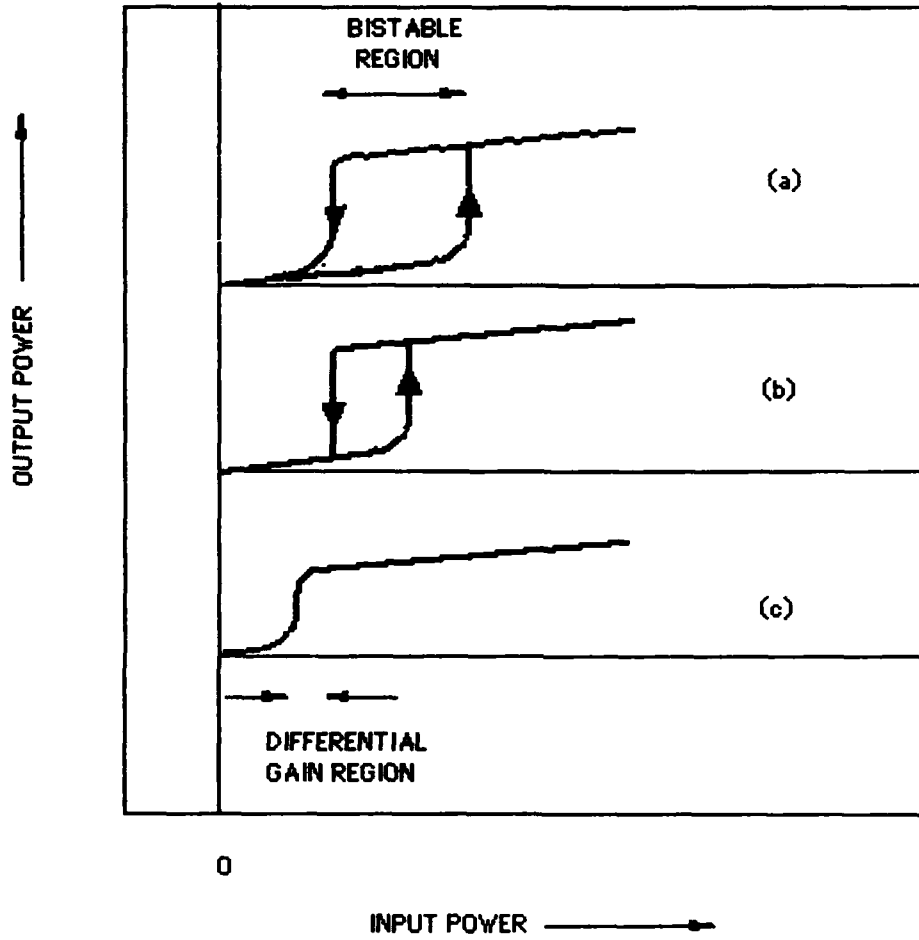
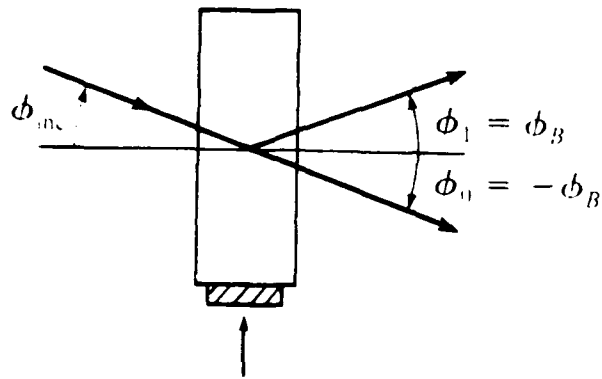
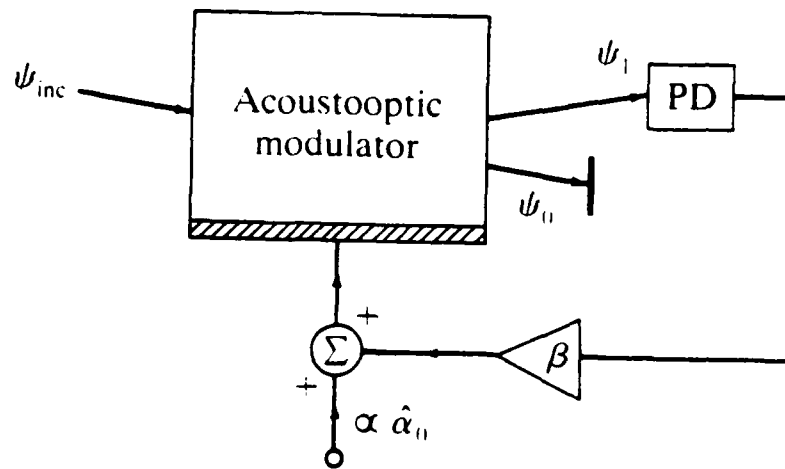


Figure 1



(a)



(b)

Figure 2

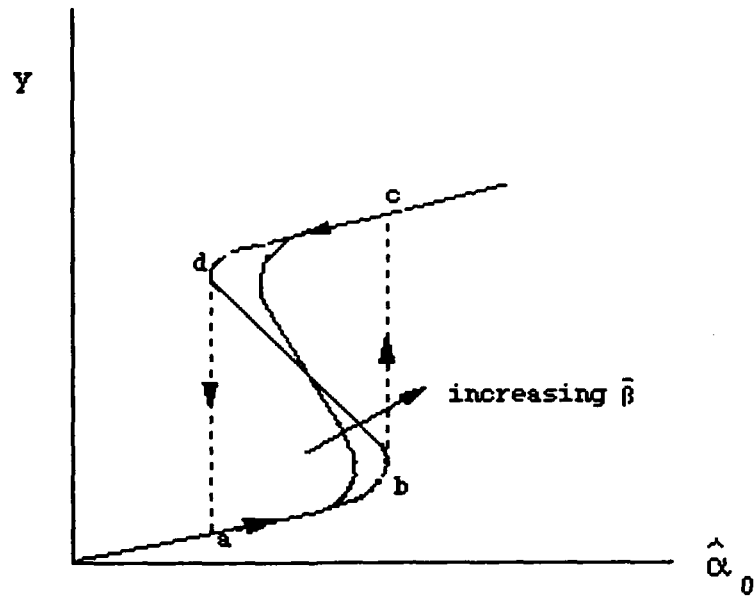


Figure 3

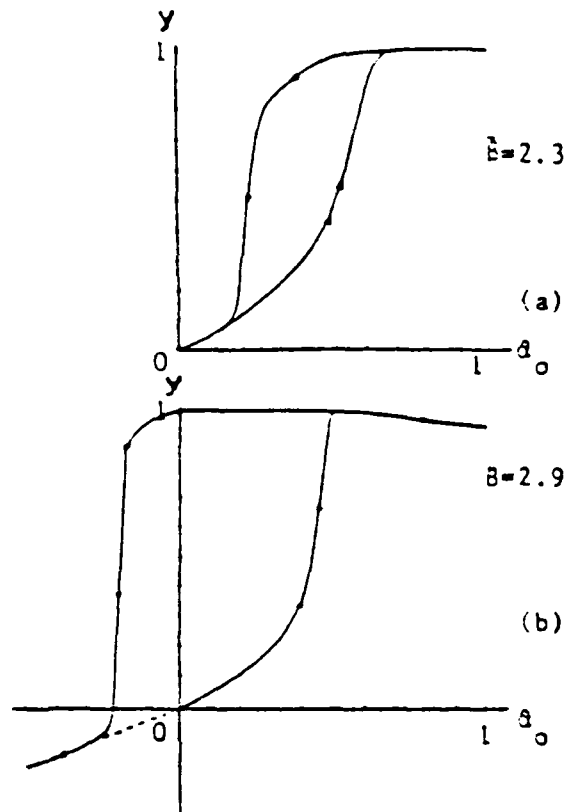


Figure 4

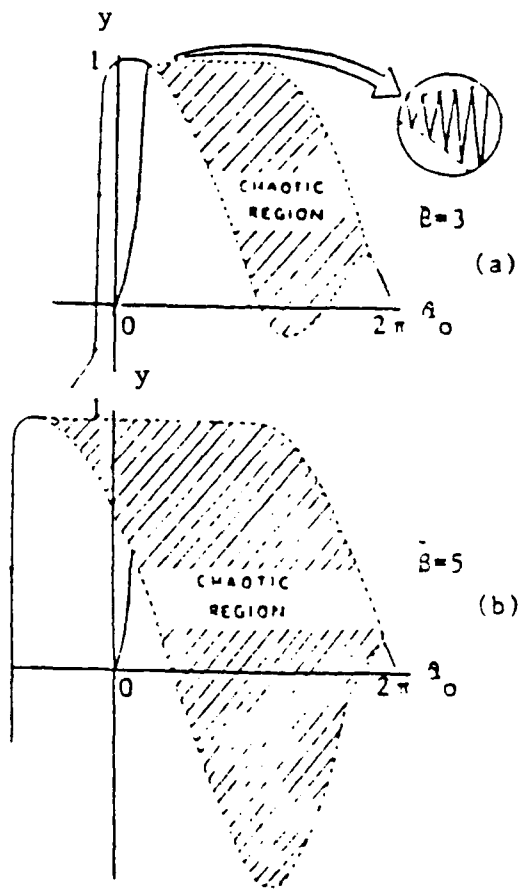


Figure 5

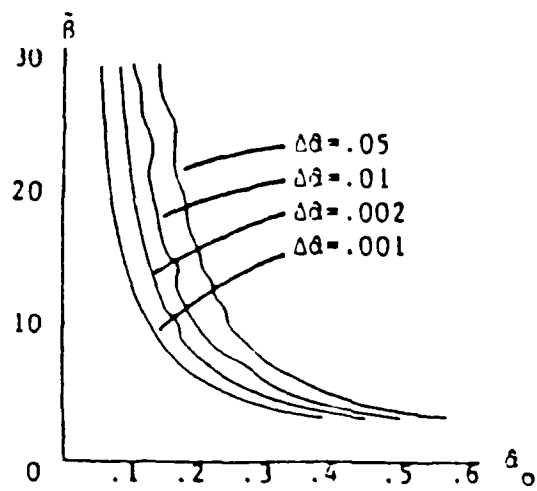


Figure 6

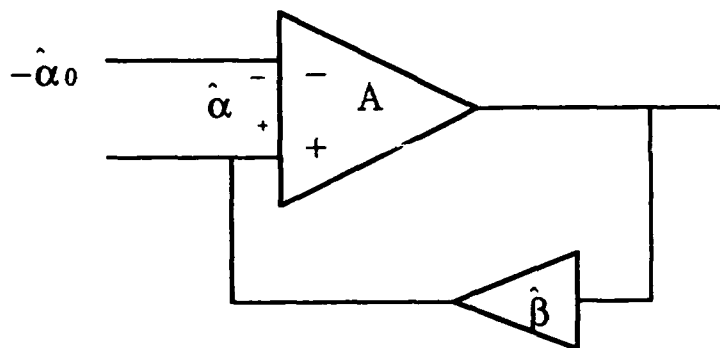


Figure 7

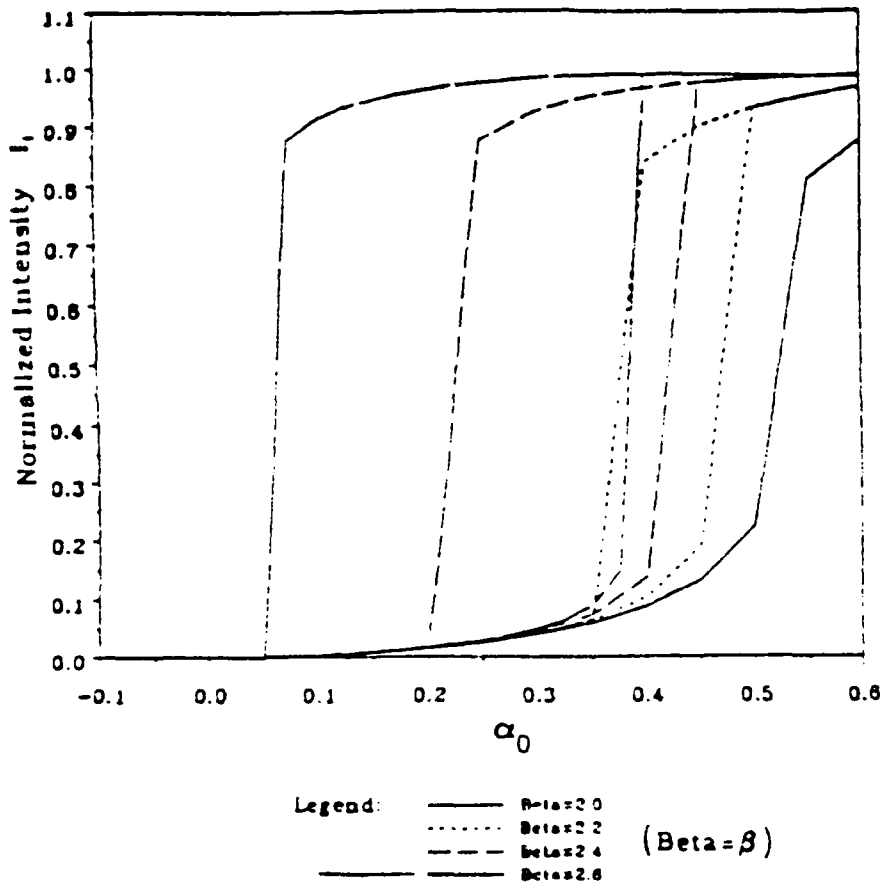
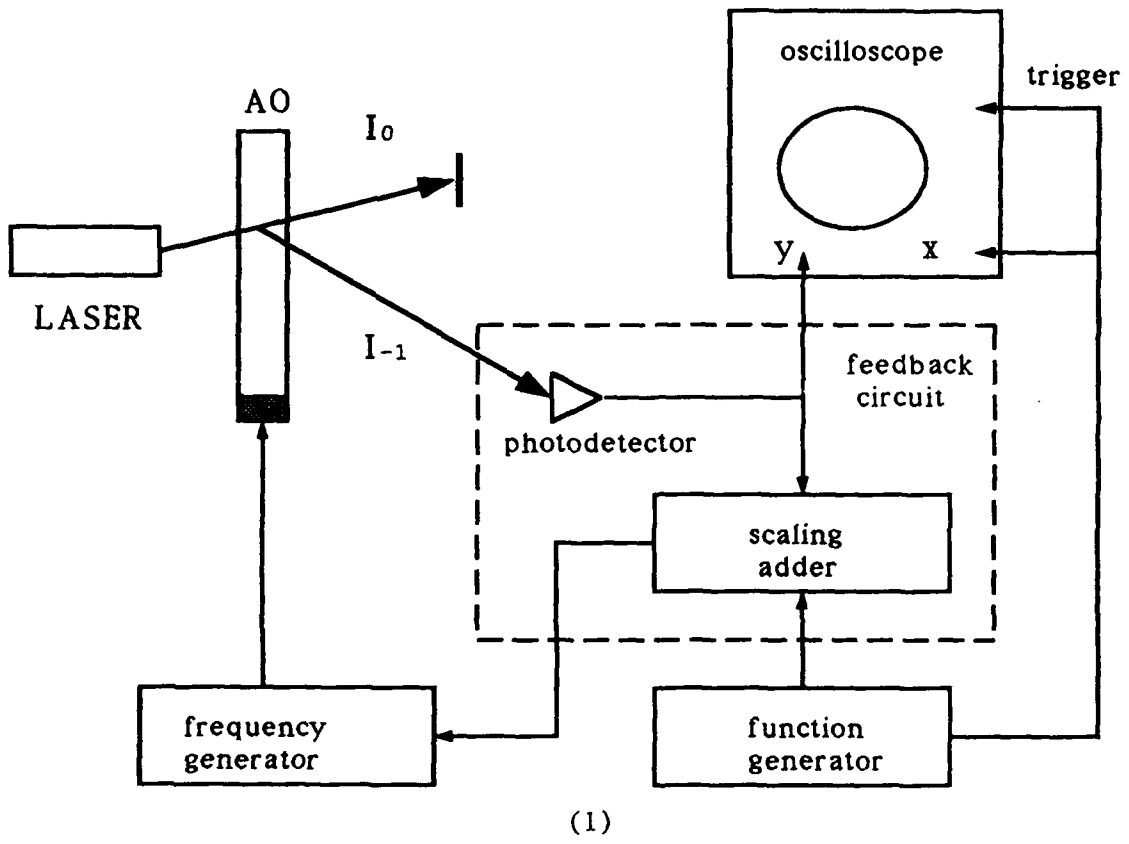
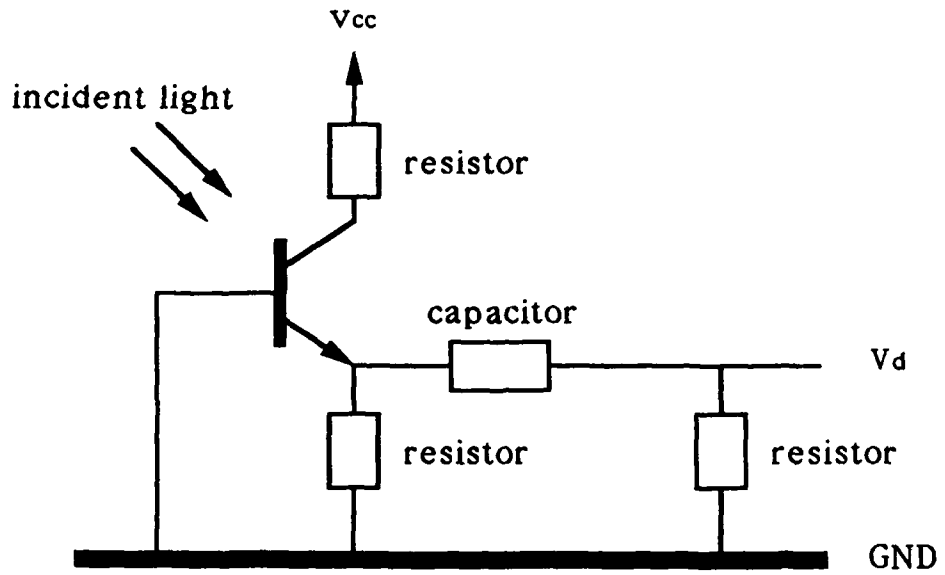


Figure 8



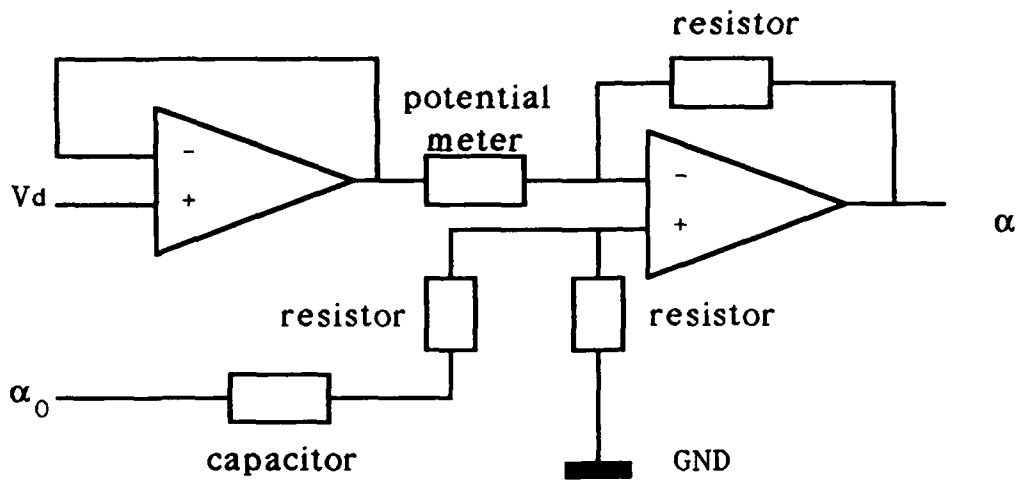
(1)

Figure 9-1



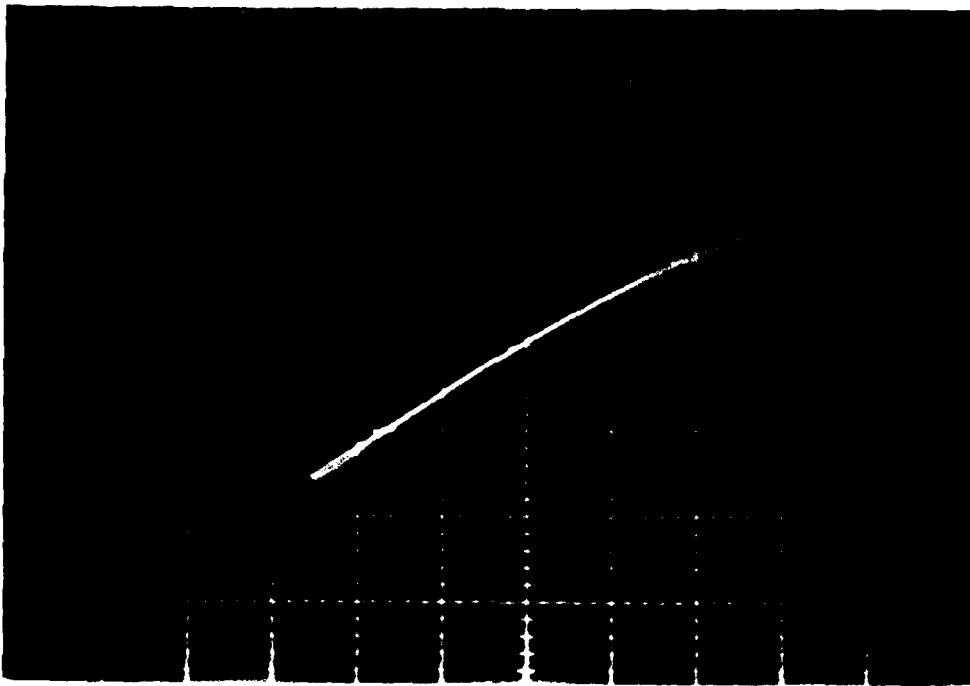
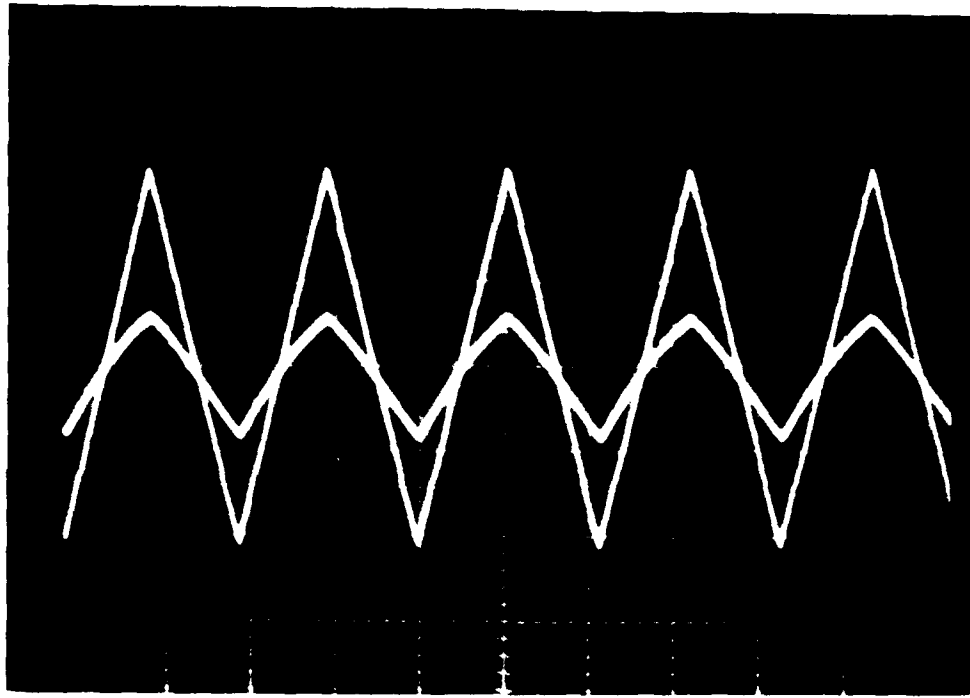
(2)

Figure 9-2



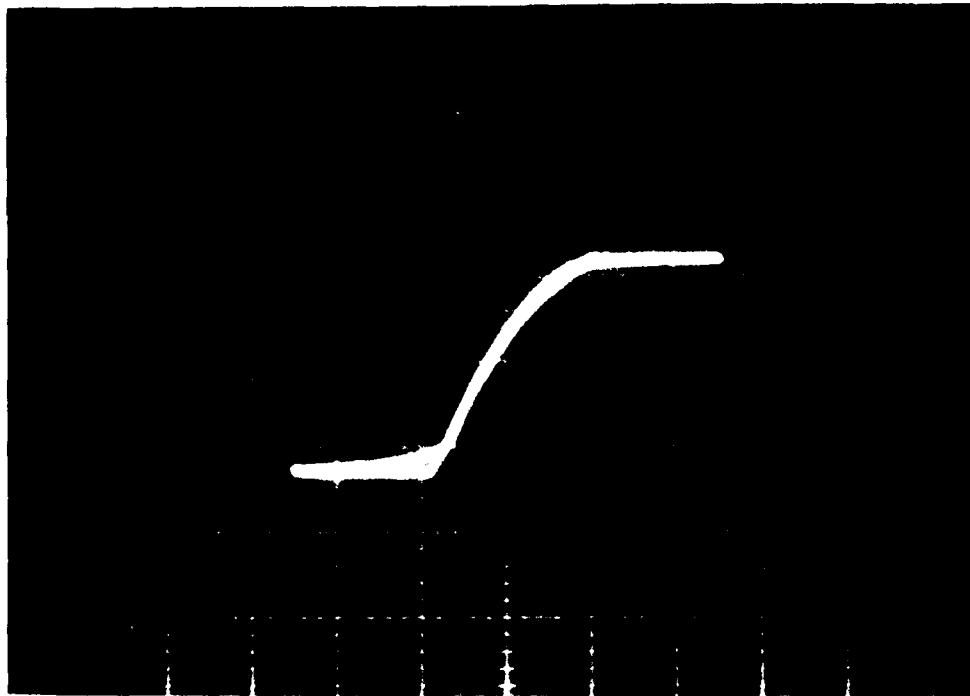
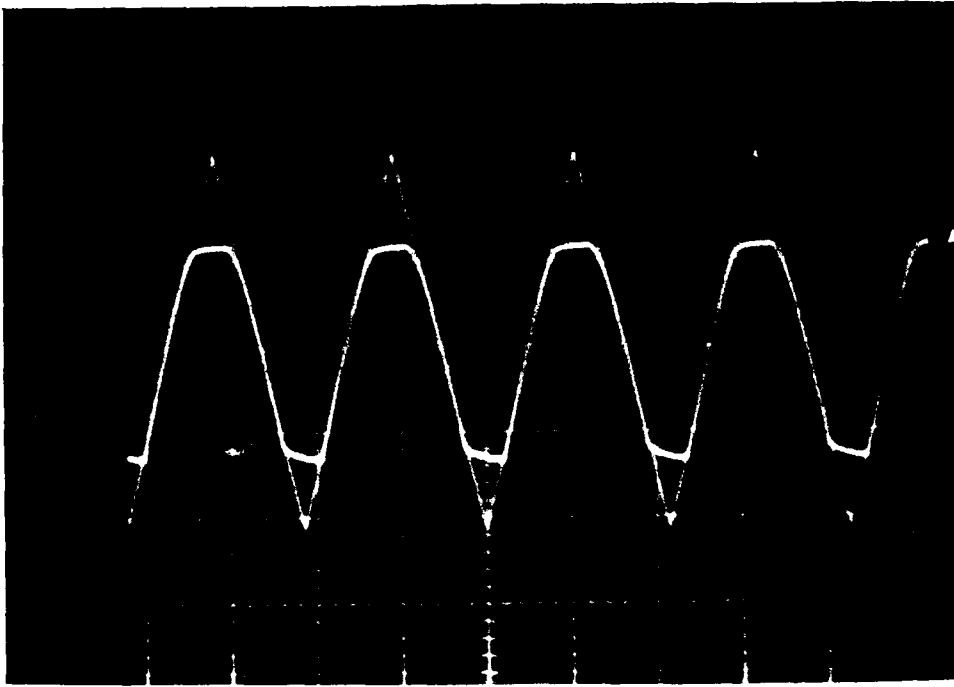
(3)

Figure 9-3



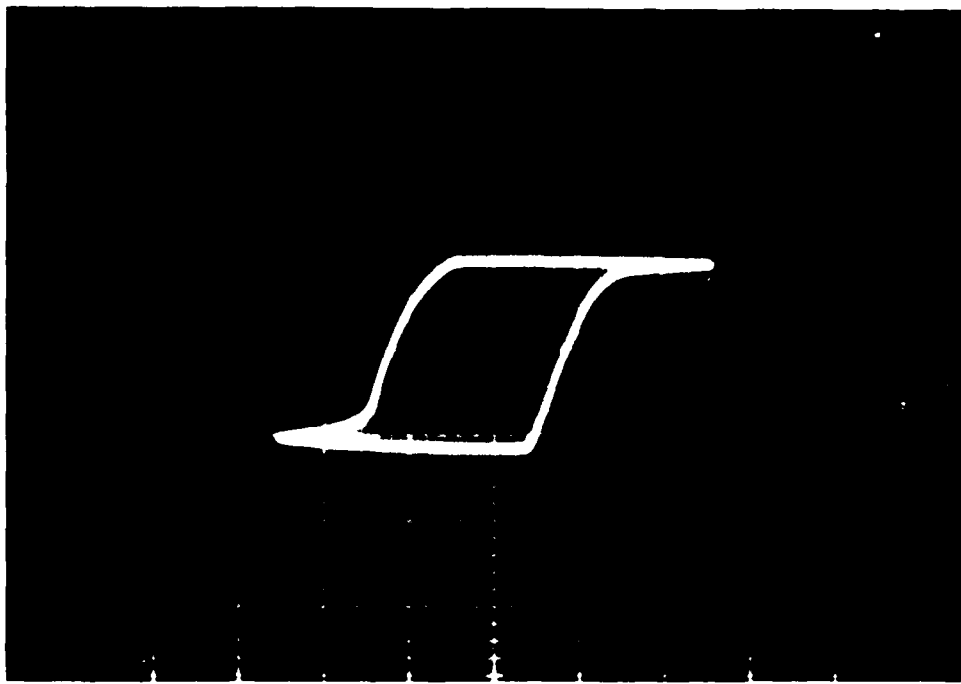
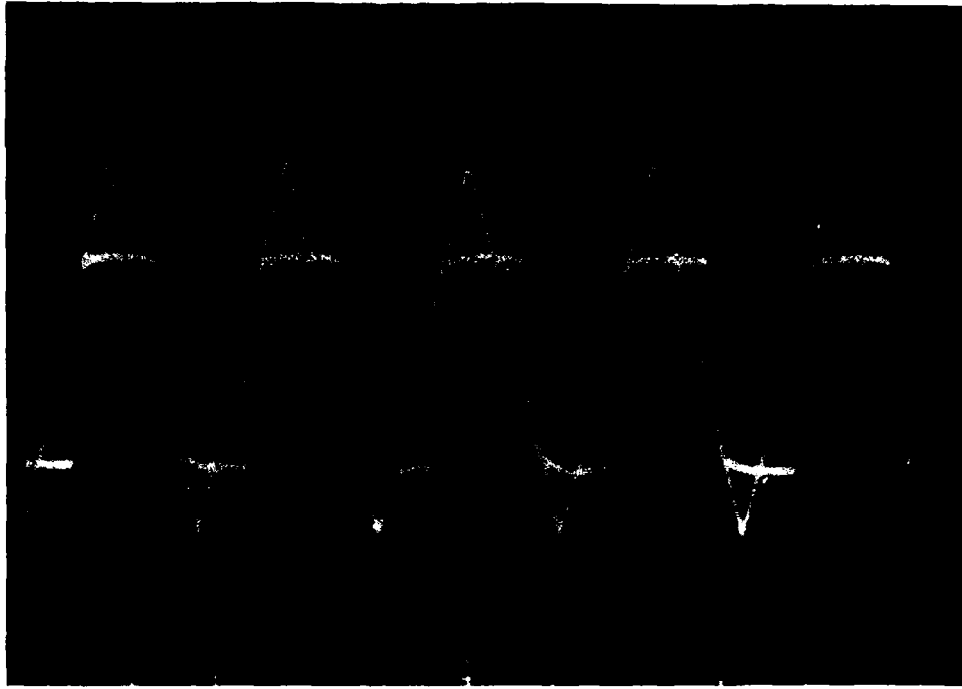
(a)

Figure 10



(b)

Figure 10



(c)

Figure 10

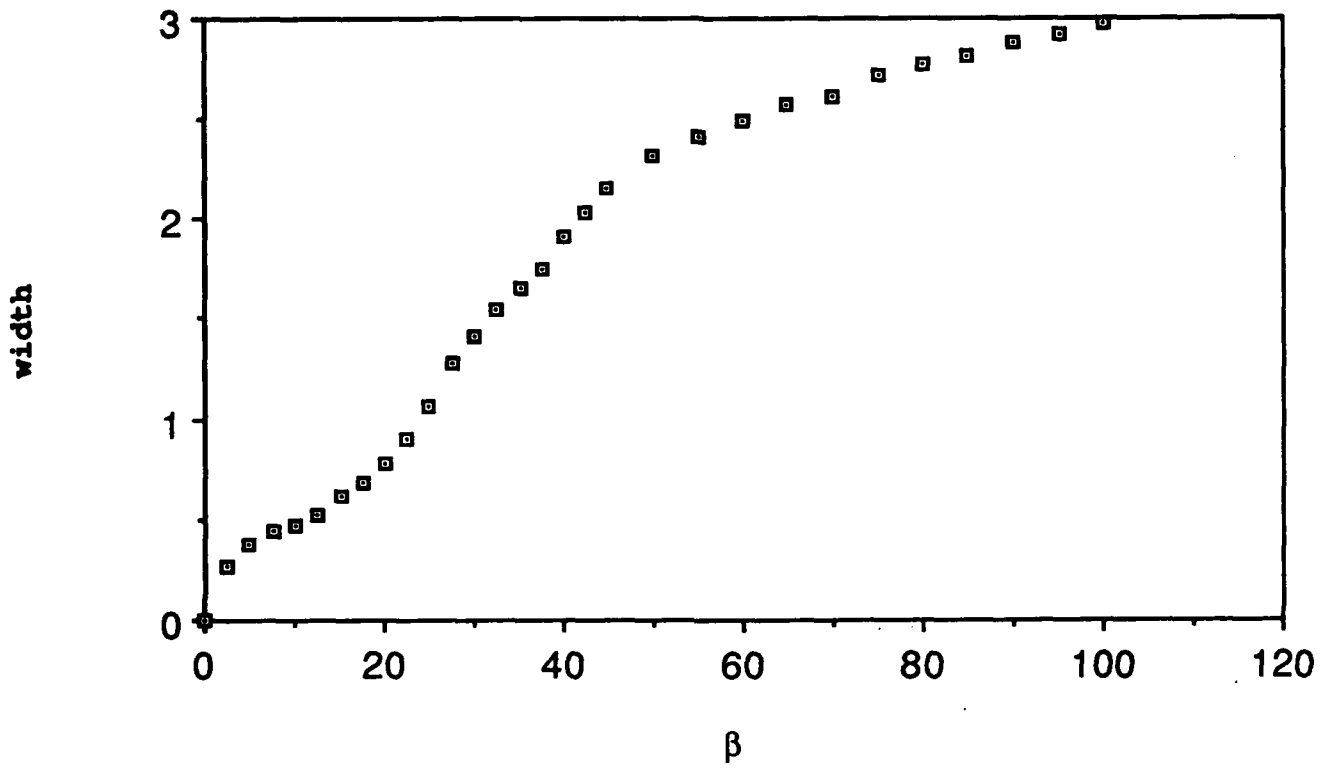


Figure 11

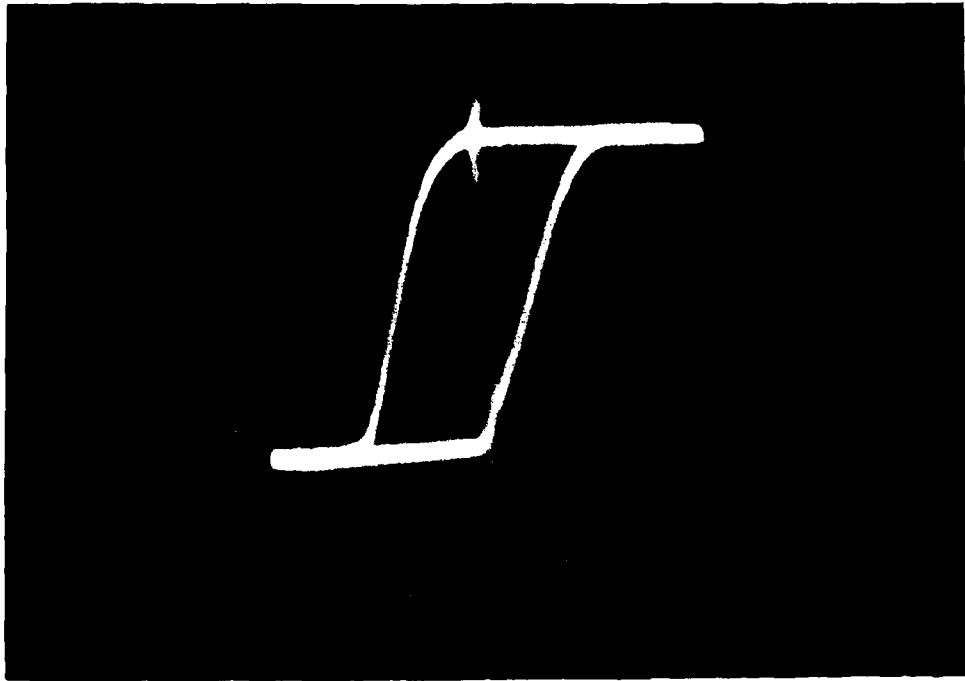


Figure 12

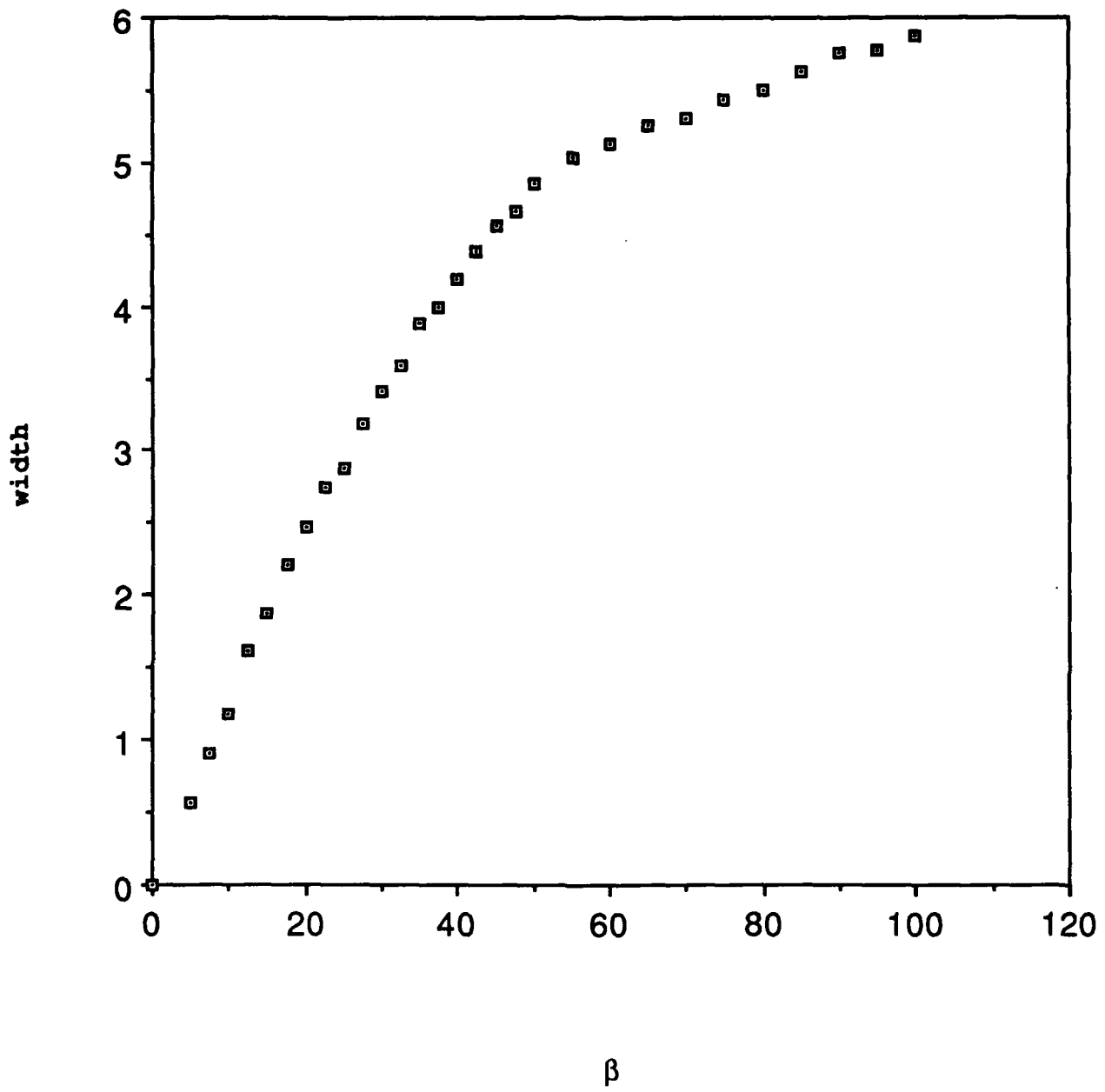


Figure 13

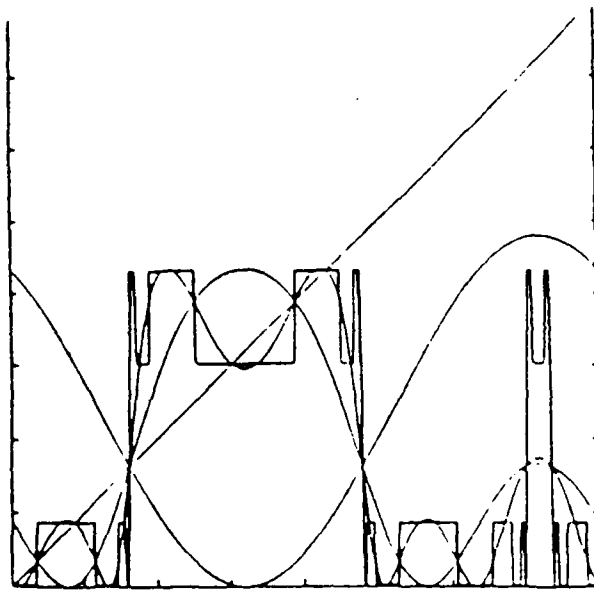


Figure 14

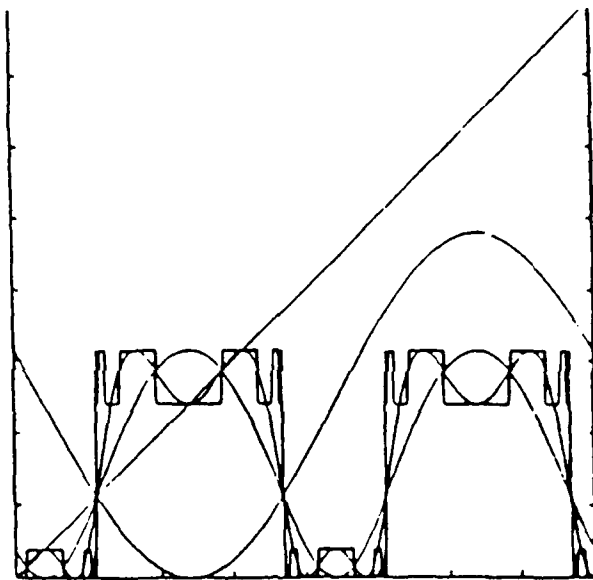


Figure 15

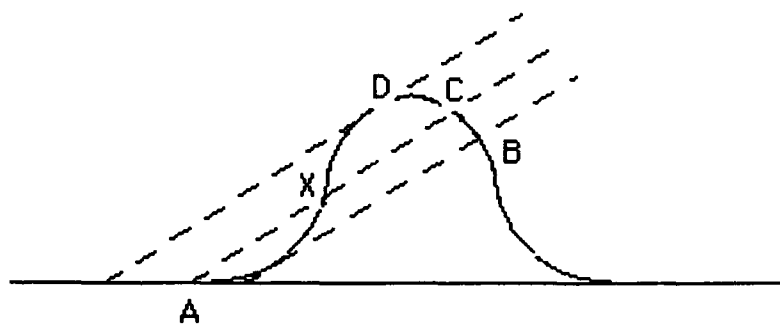


Figure 16

APPENDIX

6. APPENDIX

The ability to modulate light waves by electrical signals either through the acousto-optic or electro-optic effect provides a powerful means for optically processing information. In fact, some of the key components in modern optical processors usually consist of a spatial light modulator, such as an acousto-optic or electro-optic modulator, which is capable of spatially modulating the light beam. In this chapter, we deal with the acousto-optic and electro-optic effects. We shall also include some applications of these devices in signal processing.

6.1 Acousto-Optics

6.1.1 Qualitative Description and Heuristic Background

The interaction between sound and light is usually termed acousto-optic interaction. An acousto-optic modulator comprises an acoustic medium (such as glass or water) to which a piezoelectric transducer is bonded. Through the action of a piezoelectric transducer, the electrical signal is converted into sound waves propagating in the acoustic medium with an acoustic frequency spectrum which matches, within the bandwidth limitations of the transducer, that of the electrical excitation. The pressure in the sound wave creates a traveling wave of rarefaction and compression, which in turn causes analogous perturbations of the index of refraction. Thus, the acousto-optic device as shown in Fig 6.1 may be thought to act as a thin (phase) grating with an effective grating line separation equal to the wavelength Λ of the sound in the acoustic medium. It is well known that a grating splits incident light into various orders (see Problem 13, Chapter 3). It may be readily shown that the directions of the diffracted light inside the sound cell are governed by the following grating equation:

$$\sin \phi_m = \sin \phi_{inc} + m\lambda_o/\Lambda, \quad n = 0, \pm 1, \pm 2, \dots \quad (6.1-1)$$

where ϕ_m is the angle of the m th-order diffracted light beam, ϕ_{inc} is the angle of

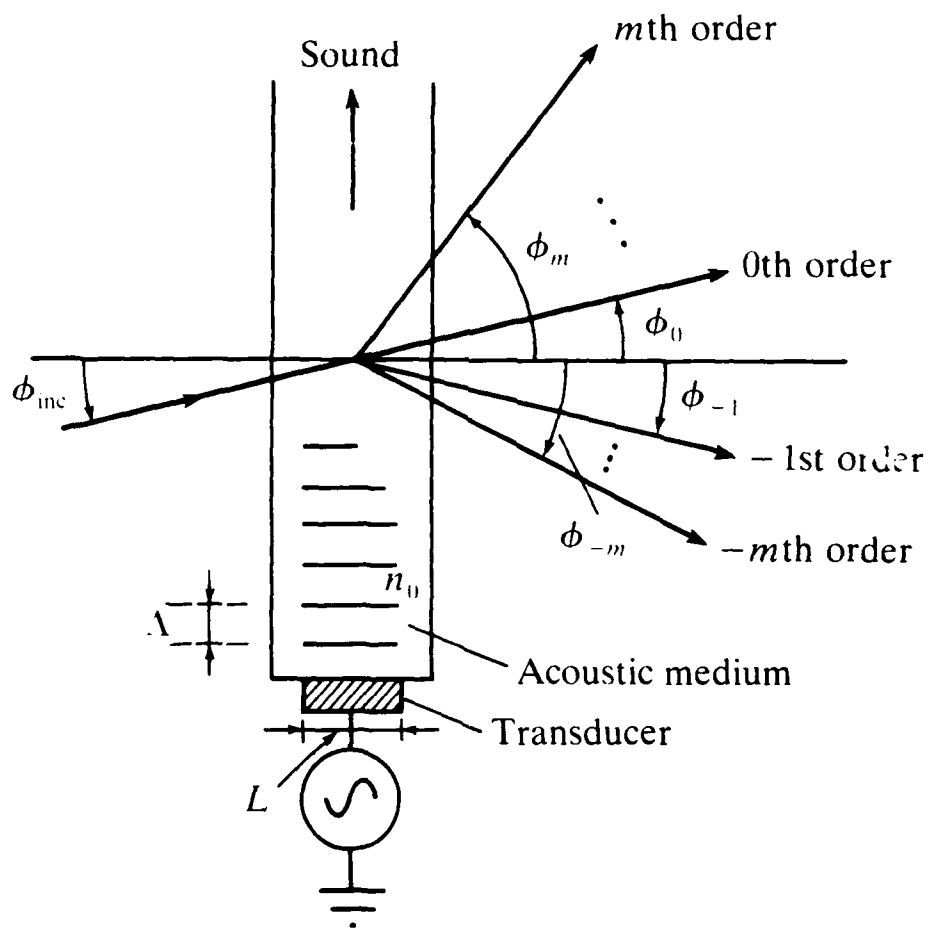


Figure 1: Basic Acoustooptic device

incidence, and λ_0 is the wavelength of light, all in the acoustic medium. Hence, the angle between neighboring order as shown in Fig. 1 equals λ_0/Λ in the cell. When measured outside the medium, these angles are increased through refraction and can be found by multiplying (6.1-1) by the refractive index n_0 of the material of the sound cell. In all figures in this chapter, pertinent angles are assumed to have been measured inside the sound cell. Since we really have a traveling sound wave, the frequencies of these diffracted beams (except the 0th-order beam) in Fig. 1 are either downshifted or upshifted by an amount equal to the sound frequency due to the Doppler effect, as will be seen later.

Through the relationship between sound wavelength Λ and sound velocity V_s in the acoustic medium ($\Lambda = 2\pi V_s/\Omega$), we can readily see that by electronically varying the sound frequency Ω , we can change the directions of propagation of the diffracted beams. It is this feature that makes it possible to use an acousto-optic device as a spectrum analyzer, as we shall see in a later section. The frequencies Ω of the "sound" waves produced in laboratories range from about 100 KHz to 3 GHz, and these sound waves are ultrasound waves whose frequencies are not audible to human ear. The range of the sound velocity in the medium lies from about 1km/s in water to about 6.5 km/s in some crystalline material such as LiNbO_3 .

As it turns out, the phase grating treatment of acousto-optic interaction is somewhat of an oversimplification in that the approach does not predict the required angle for incident light in order to obtain efficient operation, nor does it explain why only one order is generated for a sufficiently wide transducer (L large in Fig. 1).

Another, more accurate, approach considers the interaction of sound and light as a collision of photons and phonons. For these particles to have well-defined momenta and energies, we must assume that classically we have interaction of monochromatic plane waves of light and sound, i.e., we assume that the width L of the transducer is sufficiently wide in order to produce plane wavefronts at a single frequency. In the process of collision, two conservation laws have to be obeyed, namely, the conservation of energy and

momentum. If we denote the wave vectors of incident light, scattered light, and sound in the acoustic medium by \vec{k}_0 , \vec{k}_{+1} , and \vec{K} as shown in Fig. 2, we may write the condition for conservation of momentum:

$$\hbar\vec{k}_{+1} = \hbar\vec{k}_0 + \hbar\vec{K} \quad (6.1-2)$$

where $\hbar = h/2\pi$ and h denotes Planck's constant. Dividing (6.1-2) by h leads to a more convenient expression:

$$\vec{k}_{+1} = \vec{k}_0 + \vec{K}. \quad (6.1-3)$$

The corresponding conservation of energy takes the form (after division by h)

$$\omega_{+1} = \omega_0 + \Omega, \quad (6.1-4)$$

where ω_0 , Ω , and ω_{+1} are the radian frequencies of the incident light, sound, and scattered light. The interaction described by (6.1-3) is called the upshifted interaction. Fig. 2 (a) shows the wave vector interaction diagram, and Fig. 2 (b) describes the diffracted beam being upshifted in frequency. Since for all practical cases $|\vec{K}| \ll |\vec{k}_0|$, the magnitude of \vec{k}_{+1} is essentially equal to \vec{k}_0 , and therefore the wave vector momentum triangle as shown in Fig. 2 (a) is nearly isosceles.

Suppose now that we change the directions of the incident and light as shown in Fig. 3. The conservation laws can be applied again to obtain two equations similar to (6.1-3) and (6.1-4). The two equations describing the interaction are now

$$\vec{k}_{-1} = \vec{k}_0 - \vec{K}. \quad (6.1-5)$$

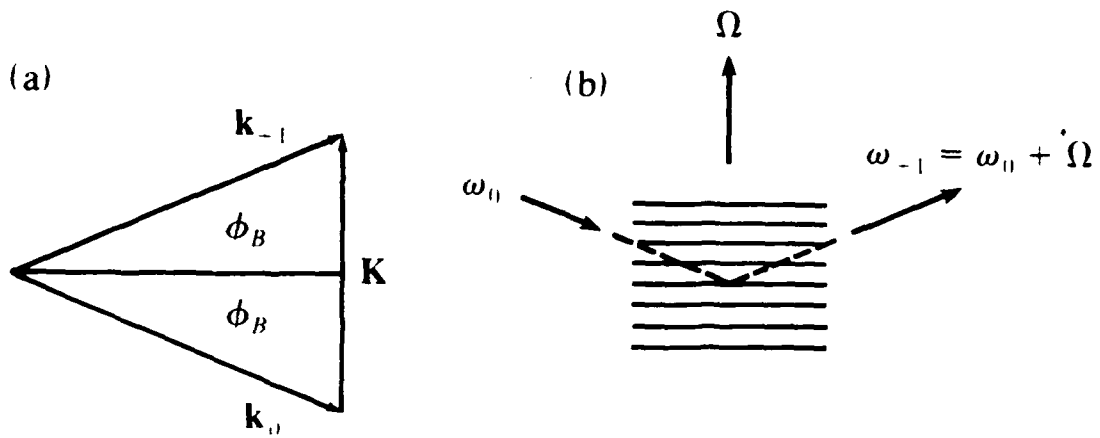


Figure 2: Upshifted diffraction. (a) wavevector diagram
(b) experimental configuration

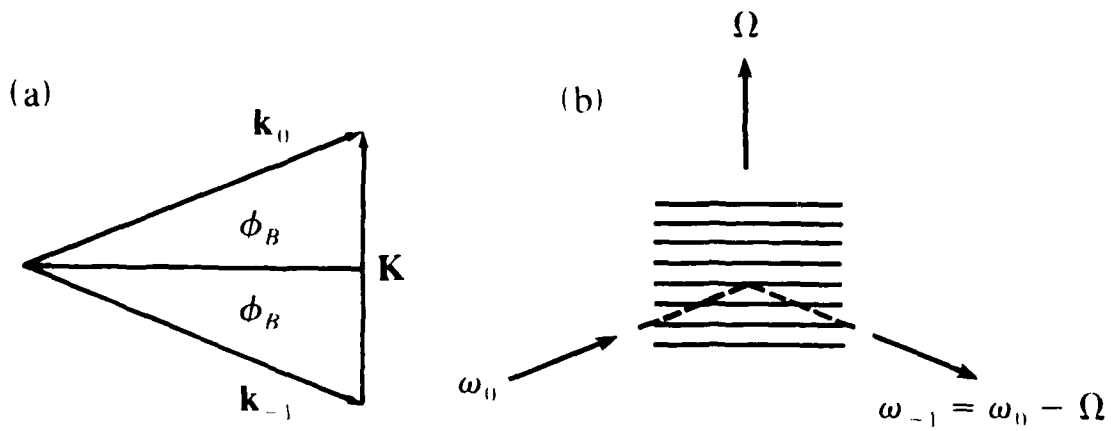


Figure 3: Downshifted diffraction. (a) wavevector diagram
(b) experimental configuration

and

$$\omega_{-1} = \omega_0 - \Omega, \quad (6.1-6)$$

where the subscripts on the LHS indicate the interaction is downshifted.

There is some interesting physics hidden in (6.1-3)–(6.1-6). It may be shown that (6.1-3) and (6.1-4) refer to phonon absorption and (6.1-5) and (6.1-6) to stimulated phonon emission. Indeed, attenuation and amplification of a sound wave have been demonstrated for these cases (see Korpel, Adler and Alpiner (1964)).

We have seen that the wave vector diagrams [Figs. 2 (a) and 3 (a)] must be closed for both cases of interaction. The closed diagrams stipulate that there are certain critical angles of incidence ($\pm\phi_B$) in the acoustic medium for plane waves of sound and light to interact, and also that the directions of the incident and diffracted light differ in angle by $2\phi_B$. The angle ϕ_B is called the Bragg angle, and this form of diffraction is called Bragg diffraction, analogous to X-ray diffraction in crystals. From Fig. 2 (a) and (b), the Bragg angle is given by

$$\sin \phi_B = K/2k_0 = \lambda_0/2\Lambda. \quad (6.1-7)$$

In actuality, scattering occurs even though the direction of incident light is not exactly at the Bragg angle. (However, the maximum diffracted intensity occurs at the Bragg angle.) The reason is that we do not have exact plane waves. The sound waves actually spread out as they propagate into the medium. As the width L of the transducer decreases, the sound column will act less and less like a single plane wave, and in fact, it is now more appropriate to consider an angular spectrum of plane waves. For a transducer with an aperture L , sound waves spread out over an angle $\pm \frac{\Lambda}{L}$, if we use the heuristic approach to diffraction (see Chapter 3). Considering the upshifted Bragg diffraction and referring to Fig. 4 we see that the \vec{K} -vector can be orientated through an angle $\pm \frac{\Lambda}{L}$ due to the spreading of sound. In order to have only one diffracted order of light generated

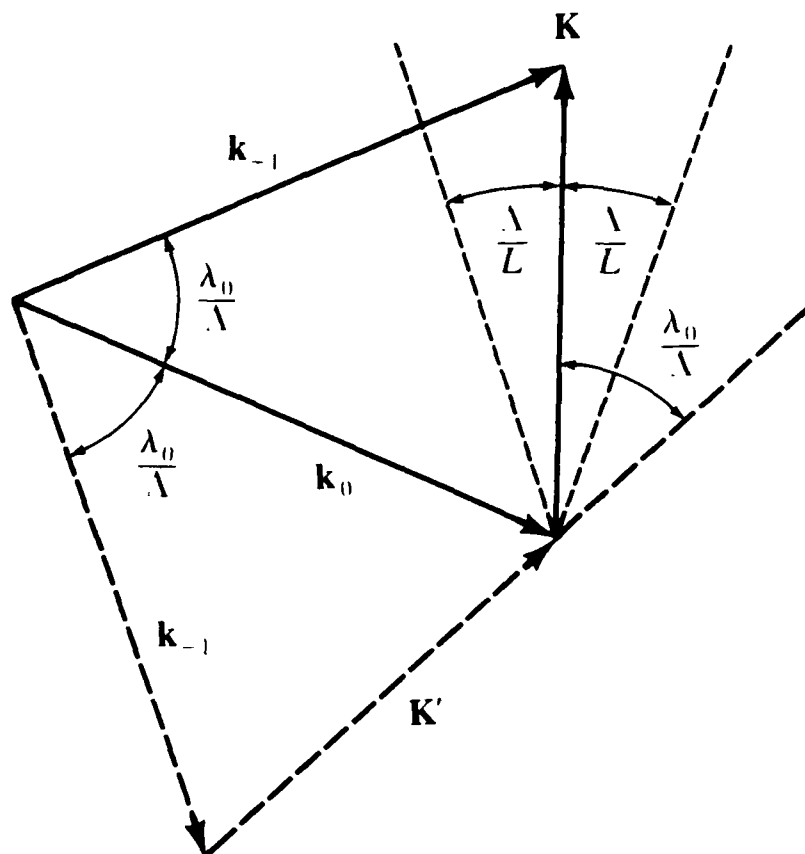


Figure 4: Wavevector diagram illustrating condition for defining Bragg regime

(i.e., \bar{k}_{+1}), we have to impose the condition:

$$\frac{\lambda_0}{\Lambda} \gg \frac{\Lambda}{L}$$

or

$$L \gg \frac{\Lambda^2}{\lambda_0}. \quad (6.1-8)$$

This is because for \bar{k}_{-1} to be generated, for example, a pertinent sound wavevector must lie along \bar{k}' ; however, this is either not present, or present in negligible amounts, in the angular spectrum of the sound, if the condition (6.1-8) is satisfied. Similar arguments may be advanced for other diffracted orders. If L satisfies the above condition, the acousto-optic device is said to be operated in the Bragg regime and the device is commonly known as the "Bragg cell."

In the case where L is sufficiently short, we have the second form of diffraction (scattering) called Raman-Nath (or Debye-Sears) diffraction. The condition

$$L \ll \frac{\Lambda^2}{\lambda_0}, \quad (6.1-9)$$

therefore, defines the Raman-Nath diffraction regime.

In Raman-Nath diffraction, \bar{k}_{+1} and \bar{k}_{-1} (i.e., positive and negative first order diffracted light) are generated simultaneously because various directions of plane waves of sound are provided from a small-aperture transducer. So far we have only considered the so-called weak interaction between the sound and incident light. i.e., the interaction between the scattered light and sound has been ignored. Scattered light may interact with the sound field again and produce higher orders of diffracted light. Whenever the rescattering process is considered in the analysis, we are well into the so-called strong interaction. [In Bragg regime, for strong interaction, scattered light \bar{k}_{+1} may rescatter back into the zero order light.] In the Raman-Nath regime, many orders may exist

because plane waves of sound are available at the various angles required for scattering.

The principle of the generation of many orders by rescattering is illustrated in Fig. 5.

\bar{K}_{+1} is generated through the diffraction of \bar{K}_0 by \bar{K}_{+1} and \bar{K}_{+2} is generated through the diffraction of \bar{K}_{+1} by \bar{K}_{+2} and so on, where the $\bar{K}_{\pm p}$'s denote the appropriate components of the plane wave spectrum of the sound. Again, the requirement of conservation of energy leads to the equation $\omega_m = \omega_0 \pm m\Omega$ with ω_m being the frequency of the mth-order scattered light.

6.1.2 The Acousto-Optic Effect

General Formalism

The interaction between the optical field $\bar{E}_0(\bar{r},t)$ and sound field $S(\bar{r},t)$ may be generally described by the Maxwell's equations. We assume the interaction takes place in a homogeneous, isotropic medium, characterized by permeability μ_0 and permittivity ϵ_0 . A source free optical field is assumed to be incident on a time varying permittivity. The time-varying permittivity is written as

$$\epsilon(\bar{r},t) = \epsilon_0 + \epsilon'(\bar{r},t), \quad (6.1-10)$$

where $\epsilon'(\bar{r},t) = \epsilon_0 C S(\bar{r},t)$, i.e., it is proportional to the sound field amplitude $S(\bar{r},t)$ with C the proportionality constant, dependent on the medium. Hence $\epsilon'(\bar{r},t)$ represents the action of the sound field. The analysis presented below closely follows the work by Korpel (1972).

We shall assume $\bar{E}_{inc}(\bar{r},t)$ satisfies the Maxwell's equations in (3.1-1) to (3.1-4) with $\rho = 0$ and $\bar{J}_c = 0$. When the sound field interacts with $\bar{E}_{inc}(\bar{r},t)$, the total field $\bar{E}(\bar{r},t)$ must satisfy the following set of equations:

$$\bar{\nabla} \times \bar{E}(\bar{r},t) = -\mu_0 \frac{\partial \bar{H}(\bar{r},t)}{\partial t}, \quad (6.1-11)$$

$$\bar{\nabla} \times \bar{H}(\bar{r},t) = \frac{\partial}{\partial t} [\epsilon(\bar{r},t) \bar{E}(\bar{r},t)], \quad (6.1-12)$$

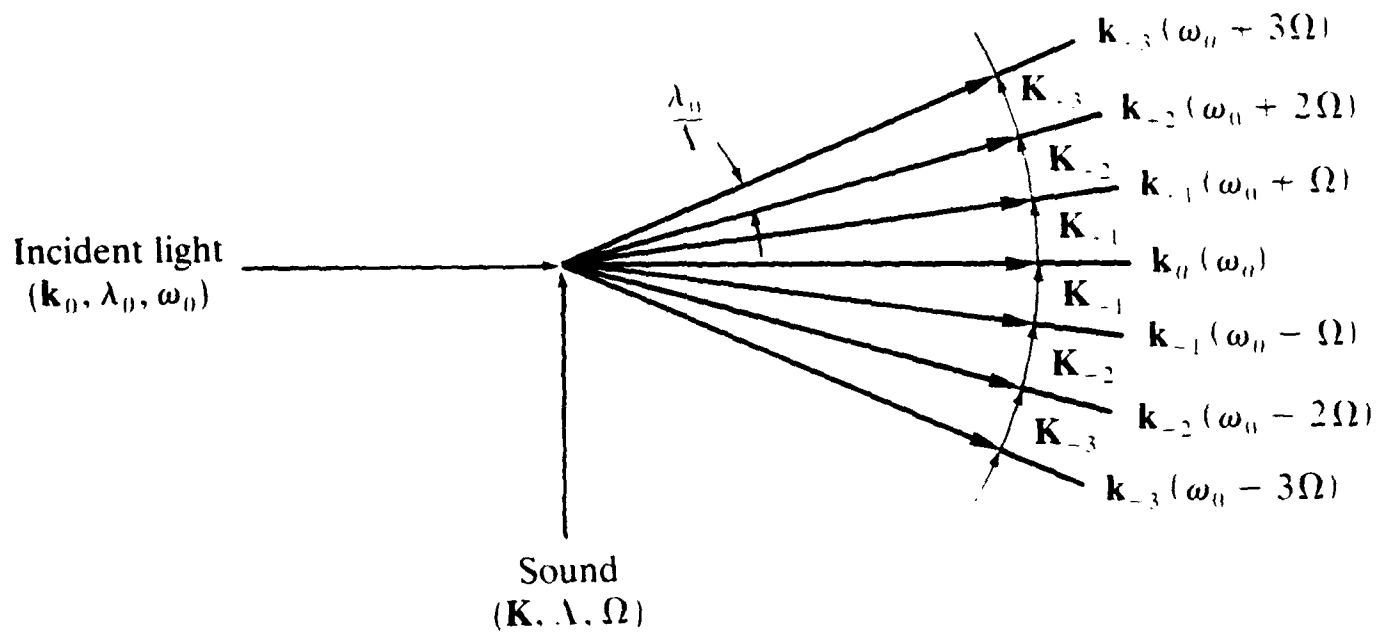


Figure 5: Multiple scattering in the Raman Nath regime

$$\bar{\nabla} \cdot [\epsilon(\bar{r},t)\bar{E}(\bar{r},t)] = 0, \quad (6.1-13)$$

$$\bar{\nabla} \cdot \bar{H}(\bar{r},t) = 0, \quad (6.1-14)$$

where $\bar{E}(\bar{r},t) = \bar{E}_{\text{inc}}(\bar{r},t) + \bar{E}'(\bar{r},t)$ with $\bar{E}'(\bar{r},t)$ defined as the scattered field.

Taking the curl of (6.1-11) and introducing it into (6.1-12), the equation for $\bar{E}(\bar{r},t)$ reads

$$\begin{aligned} \bar{\nabla} \times \bar{\nabla} \times \bar{E}(\bar{r},t) &= \bar{\nabla}(\bar{\nabla} \cdot \bar{E}) - \bar{\nabla}^2 \bar{E} \\ &= -\mu_0 \frac{\partial^2}{\partial t^2} [\epsilon(\bar{r},t) \bar{E}(\bar{r},t)] \end{aligned} \quad (6.1-15)$$

Now, from (6.1-15), we have

$$\bar{\nabla} \cdot \epsilon \bar{E} = \epsilon \bar{\nabla} \cdot \bar{E} + \bar{E} \cdot \bar{\nabla} \epsilon = 0 \quad (6.1-16)$$

Assuming a 2-D (xz) configuration with \bar{E} polarized along the y-direction, it can be readily shown that $\bar{E} \cdot \bar{\nabla} \epsilon = 0$; hence (6.1-15) reduces to

$$\bar{\nabla}^2 \bar{E}(\bar{\rho},t) = \mu_0 \frac{\partial^2}{\partial t^2} [\epsilon(\bar{\rho},t) \bar{E}(\bar{\rho},t)], \quad (6.1-17)$$

where $\bar{\rho}$ is the position vector in the xz plane, and $\bar{E}(\bar{\rho},t) = E(\bar{\rho},t) \hat{a}_y$. The term on the right hand side of (6.1-17) may be written as

$$\mu_0 \left[E \frac{\partial^2 \epsilon}{\partial t^2} + 2 \frac{\partial E}{\partial t} \frac{\partial \epsilon}{\partial t} + \epsilon \frac{\partial^2 E}{\partial t^2} \right]. \quad (6.1-18)$$

Since the time variation of $\epsilon(\bar{\rho},t)$ is much slower than that of $E(\bar{\rho},t)$, we may only retain the last term in (6.1-18) to get, using (6.1-10) and (6.1-17),

$$\bar{\nabla}^2 \bar{E}(\bar{\rho},t) - \mu_0 \epsilon_0 \frac{\partial^2 \bar{E}(\bar{\rho},t)}{\partial t^2} = \mu_0 \epsilon'(\bar{\rho},t) \frac{\partial^2 \bar{E}(\bar{\rho},t)}{\partial t^2}, \quad (6.1-19)$$

Eq. (6.1-19) is the one most used to investigate strong interaction in acousto-optics.

We shall now introduce harmonic variations in the light and sound in the form of

$$E_{\text{inc}}(\bar{\rho}, t) = \frac{1}{2} E_{\text{inc}}(\bar{\rho}) e^{j\omega_0 t} + \text{c.c.}, \quad (6.1-20)$$

and

$$\frac{\epsilon'(\bar{\rho}, t)}{\epsilon_0} = \frac{1}{2} C S(\bar{\rho}) e^{j\Omega t} + \text{c.c.}, \quad (6.1-21)$$

where c.c. denotes the complex conjugate. Since we have harmonic fields, we may anticipate, as seen in the simplified analysis before in Section 6.1.1, frequency mixing due to the interaction. We shall then cast the total field $E(\bar{\rho}, t)$ into the following form:

$$E(\bar{\rho}, t) = \sum_{m=-\infty}^{\infty} \frac{1}{2} E_m(\bar{\rho}) e^{j(\omega_0 + m\Omega)t} + \text{c.c.} \quad (6.1-22)$$

Substituting (6.1-20) – (6.1-22) into (6.1-19) and assuming $\Omega \ll \omega_0$, we obtain, after some straightforward calculations, the following infinite coupled-wave system:

$$\bar{\nabla}^2 E_m(\bar{\rho}) + k_0^2 E_m(\bar{\rho}) + \frac{1}{2} k_0^2 C S(\bar{\rho}) E_{m-1}(\bar{\rho}) + \frac{1}{2} k_0^2 C S^*(\bar{\rho}) E_{m+1}(\bar{\rho}) = 0, \quad (6.1-23)$$

where $k_0 = \omega_0 \sqrt{\mu_0 \epsilon_0}$ is the light propagation in the medium, and the asterisk denotes the complex conjugate. Note that $E_m(\bar{\rho})$ is the amplitude of the m th-order light at frequency $\omega_0 + m\Omega$.

Sound Field Configuration and Plane Wave Interaction Model

We shall now consider a conventional interaction configuration depicted in Fig 6. As we can see, a uniform sound plane wave along z of finite length is often used and we shall represent the sound by

$$S(\bar{\rho}) = S(z, x) = A e^{-jKx}, \quad (6.1-24)$$

where A , in general, may be complex. The incident plane wave of light by may be represented as

$$E_{\text{inc}}(\bar{\rho}) = \psi_{\text{inc}} e^{-jk_0 z \cos \phi_{\text{inc}}} e^{-jk_0 x \sin \phi_{\text{inc}}}, \quad (6.1-25)$$

where ϕ_{inc} is the incident angle. We look for a solution of the form

$$E_m(\bar{\rho}) = E_m(z, x) = \psi_m(x, z) e^{-jk_0 z \cos \phi_m} e^{-jk_0 x \sin \phi_m} \quad (6.1-26)$$

with the choice for ϕ_m given by (6.1.1):

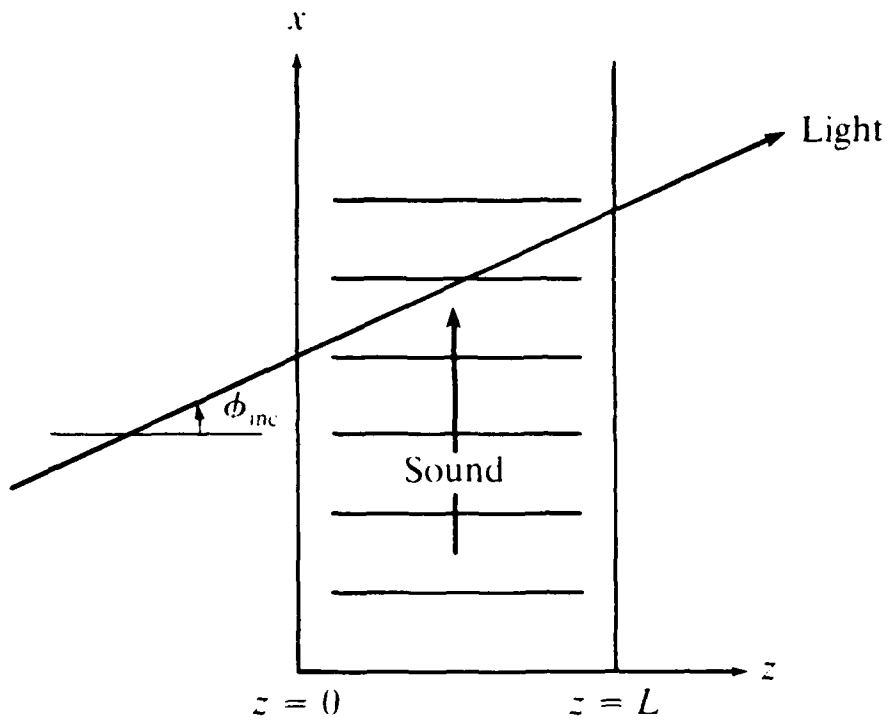


Figure 6: Conventional light-sound interaction configuration

$$\sin \phi_m = \sin \phi_{inc} + m \frac{\lambda_0}{\Lambda} = \sin \phi_{inc} + m \frac{K}{k_0} \quad (6.1-27)$$

Substituting (6.1-24), (6.1-26) and (6.1-27) into (6.1-23), we obtain, after some algebra,

$$\begin{aligned} & \frac{\partial^2 \psi_m}{\partial x^2} + \frac{\partial^2 \psi_m}{\partial z^2} - 2jk_0 \sin \phi_m \frac{\partial \psi_m}{\partial x} - 2jk_0 \cos \phi_m \frac{\partial \psi_m}{\partial z} \\ & + \frac{1}{2} k_0^2 CA^* \psi_{m+1} e^{-jk_0 z (\cos \phi_{m+1} - \cos \phi_m)} + \frac{1}{2} k_0^2 CA \psi_{m-1} e^{-jk_0 z (\cos \phi_{m-1} - \cos \phi_m)} = 0. \end{aligned} \quad (6.1-28)$$

From (6.1-28) we see that ϕ_m is a very small quantity if $\phi_{inc} \ll 1$ justifying the assumption $\psi_m(z, x) \approx \psi_m(z)$. Also, we assume that within a wavelength of light, $\partial \psi_m / \partial z$ does not change appreciably; hence $\partial^2 \psi_m / \partial z^2$ can be neglected when compared to $2jk_0 \cos \phi_m \partial \psi_m / \partial z$. Eq. (6.1-28) then becomes

$$\begin{aligned} \frac{d\psi_m}{dz} &= \frac{-jk_0 CA}{4 \cos \phi_m} \psi_{m-1} e^{-jk_0 z (\cos \phi_{m-1} - \cos \phi_m)} \\ &+ \frac{-jk_0 CA^*}{4 \cos \phi_m} \psi_{m+1} e^{-jk_0 z (\cos \phi_{m+1} - \cos \phi_m)}, \end{aligned} \quad (6.1-29)$$

with the boundary conditions

$$\psi_m = \psi_{inc} \delta_{m0} \text{ at } z \leq 0, \quad (6.1-30)$$

where δ_{m0} represents the Kronecker delta function.

The physical interpretation to (6.1-29) is that there is a mutual coupling between neighboring orders in the interaction, i.e., ψ_m is being contributed to by ψ_{m-1} and ψ_{m+1} . However, the phase of the contributions varies with z , and the exponents with arguments $k_0 z (\cos \phi_{m-1} - \cos \phi_m)$ and $k_0 z (\cos \phi_{m+1} - \cos \phi_m)$ represent the lack of phase synchronism in this coupling process.

Raman-Nath Regime

As mentioned before, Raman-Nath diffraction is characterized by the simultaneous generation of many diffracted orders. This implies that the interaction length L must be short enough such that the accumulated degree of phase mismatch between ψ_m and its

neighboring orders, as given by the arguments of the exponential terms in (6.1-29) is small. Assuming small values of K/k_0 , the phase-asynchronism terms $k_0 z(\cos\phi_{m-1} - \cos\phi_m)$ and $k_0 z(\cos\phi_{m+1} - \cos\phi_m)$ in (6.1-29) can be expanded in a power series by using (6.1-27)

$$k_0 z(\cos\phi_{m-1} - \cos\phi_m) = k_0 z \left[\left(\frac{K}{k_0}\right) \sin\phi_{inc} + (m - \frac{1}{2}) \left(\frac{K}{k_0}\right)^2 + \dots \right] \quad (6.1-31)$$

$$k_0 z(\cos\phi_{m+1} - \cos\phi_m) = k_0 z \left[-\left(\frac{K}{k_0}\right) \sin\phi_{inc} - (m + \frac{1}{2}) \left(\frac{K}{k_0}\right)^2 + \dots \right] \quad (6.1-32)$$

For $\phi_{inc} = 0$, the accumulated phase mismatch for order m at $z=L$ is negligible if

$$m(K^2/k_0)L \ll 1. \quad (6.1-33)$$

This condition is the criterion for an acousto-optic device operated in the Raman-Nath regime. It is usually stated with $m=1$ and is consistent with (6.1-9).

Using the above criterion and assuming $\phi_m \ll 1$, (6.1-29) becomes

$$\frac{d\psi_m}{dz} = -\frac{jk_0 CA}{4} \psi_{m-1} - \frac{jk_0 CA^*}{4} \psi_{m+1}. \quad (6.1-34)$$

For simplicity, let $A = A^* = |A|$, where $|A|$ represents the peak strain caused by the sound field $|A| \cos(\Omega t - Kx)$ [See (6.1-21) and (6.1-24)], and we may write for (6.1-34):

$$\frac{d\psi_m}{dz} = \frac{-jk_0 C |A|}{4} \left[\psi_{m-1} + \psi_{m+1} \right]. \quad (6.1-35)$$

The solution to (6.1-35) is readily given by considering the recurrence relation for the Bessel function:

$$\frac{dJ_m(z)}{dz} = \frac{1}{2} \left[J_{m-1}(z) - J_{m+1}(z) \right], \quad (6.1-36)$$

and writing $\psi_m = (-j)^m \psi'_m$, where $\psi'_m = J_m \left(\frac{k_0 C |A| z}{2} \right)$. It follows immediately, with (6.1-30), that the amplitude of the various diffracted orders inside the sound column at $z=L$ is

$$\psi_m = (-j)^m \psi_{\text{inc}} J_m \left(\frac{k_0 C |A| L}{2} \right), \quad (6.1-37)$$

which is the well-known Raman-Nath solution, plotted in Fig. 6.8(a)

Bragg Regime

As pointed out before, Bragg diffraction is characterized by the generation of two diffracted orders. Referring to (6.1-29), we find that for the diffracted orders 0 and -1 (downshifted interaction), the coupled equations read:

$$\frac{d\psi_0}{dz} = \frac{-jk_0 CA}{4\cos\phi_0} \psi_{-1} e^{-jk_0 z(\cos\phi_{-1} - \cos\phi_0)}, \quad (6.1-38a)$$

and

$$\frac{d\psi_{-1}}{dz} = \frac{-jk_0 CA^*}{4\cos\phi_{-1}} \psi_0 e^{+jk_0 z(\cos\phi_{-1} - \cos\phi_0)}. \quad (6.1-38b)$$

Assuming phase synchronism between the 0th and -1st order, we must impose $\cos\phi_{-1} = \cos\phi_0$, implying

$$\phi_{-1} = -\phi_0, \quad (6.1-39)$$

as $\phi_{-1} \neq \phi_0$, since different scattered orders must exit at different angles. Hence, referring to Fig. 7a it readily follows that

$$\begin{aligned} \phi_0 &= \phi_B = \phi_{\text{inc}} \\ \phi_{-1} &= -\phi_B = -\phi_{\text{inc}}. \end{aligned} \quad (6.1-40)$$

Thus, the 0th and the diffracted (-1st) order propagate symmetrically with respect to the sound wavefronts. Similar arguments may be advanced for the upshifted interaction case.

In light of the above discussion, the coupled equations describing downshifted interaction become

$$\frac{d\psi_0}{dz} = \frac{-jk_0 CA}{4\cos\phi_B} \psi_{-1}, \quad (6.1-41)$$

$$\frac{d\psi_{-1}}{dz} = \frac{-jk_0 CA^*}{4\cos\phi_B} \psi_0. \quad (6.1-42)$$

Similarly, the coupled equations

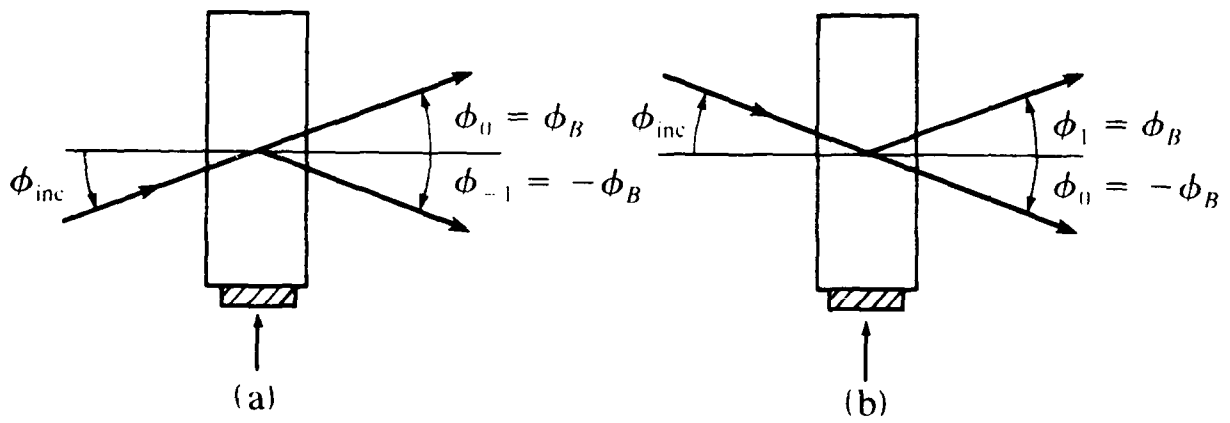


Figure 7: (a) downshifted interaction (b) upshifted interaction.

$$\frac{d\psi_0}{dz} = \frac{-jk_0 CA^*}{4\cos\phi_B} \psi_{-1} \quad (6.1-43)$$

$$\frac{d\psi_{-1}}{dz} = \frac{-jk_0 CA}{4\cos\phi_B} \psi_0 \quad (6.1-44)$$

describe upshifted diffraction ($\phi_{inc} = -K/2k_0 = -\phi_B$). Note that these equations are the standard ordinary differential equations (ODEs) for coupled modes, where the coupling coefficients are $-jk_0 CA/4\cos\phi_B$ and $-jk_0 CA^*/4\cos\phi_B$. The solutions at $z=L$, taking the boundary conditions (6.1-30) into account, and with $\phi_B \ll 1$, read

$$\begin{aligned} \psi_0 &= \psi_{inc} \cos(k_0 C|A|L/4) \\ \psi_{-1} &= -j \frac{A^*}{|A|} \psi_{inc} \sin(k_0 C|A|L/4) \end{aligned} \quad (6.1-45)$$

for the downshifted interaction, and

$$\begin{cases} \psi_0 = \psi_{inc} \cos(k_0 C|A|L/4) \\ \psi_{-1} = -j \frac{A}{|A|} \psi_{inc} \sin(k_0 C|A|L/4), \end{cases} \quad (6.1-46)$$

for the upshifted case. Eq. (6.1-45) or (6.1-46) are the well-known expressions for the scattered light in Bragg diffraction.

At this point it is instructive to relate the term $C|A|$ to a refraction-index variation $\Delta n_0(\bar{\rho}, t)$ in the acousto-optic cell. Since

$$\begin{aligned} \epsilon(\bar{\rho}, t) &= \epsilon_v n^2(\bar{\rho}, t) \\ &= \epsilon_v [n_0 + \Delta n_0(\bar{\rho}, t)]^2 \\ &\approx \epsilon_v n_0^2 [1 + 2\Delta n_0(\bar{\rho}, t)/n_0], \end{aligned} \quad (6.1-47)$$

where n_0 denotes the unperturbed refraction index of the medium, we compare (6.1-47) with (6.1-10) and obtain

$$C|S|(\bar{\rho}, t) = \frac{2\Delta n_0(\bar{\rho}, t)}{n_0}, \quad (6.1-48)$$

or $C|S| = C|A| = 2(\Delta n_0)_{max}/n_0$, where $(\Delta n_0)_{max}$ denotes the peak amplitude of the assumed harmonic variation of $\Delta n_0(\bar{\rho}, t)$. The quantity $k_0 C|A|L/2$ then can be written as

$$k_0 C |A| L/2 = k_v (\Delta n_0)_{\max} L = \hat{\alpha}, \quad (6.1-49)$$

where α represents the peak phase delay of the light through the acoustic medium and k_v is the wave number in vacuum. Summarizing the solutions to the Raman-Nath and Bragg regions in terms of $\hat{\alpha}$, we have

$$\psi_m(z) = \psi_{\text{inc}} (-j)^m J_m(\hat{\alpha}), \quad (6.1-50)$$

and

$$\begin{cases} \psi_0 = \psi_{\text{inc}} \cos(\hat{\alpha}/2) \\ \psi_{\pm 1} = -j \psi_{\text{inc}} \sin(\hat{\alpha}/2), \end{cases} \quad (6.1-51)$$

respectively, where $A = A^* = |A|$ has been assumed in writing the above equations. Fig. 8 illustrates the dependence of various diffracted orders on $\hat{\alpha}$ for the two regimes.

Finally it should be pointed out that the criterion for an acousto-optic cell to operate in the Bragg regime is the inverse relation to (6.1-33)

$$(K^2/k_0)L \gg 1, \quad (6.1-52)$$

where the strongest condition is implied (i.e., $m=1$). [Note that (6.1-52) is consistent with (6.1-8)]. In physical reality, a complete energy transfer between ψ_0 and $\psi_{\pm 1}$ is never possible as there always exists more than two orders no matter how strong condition (6.1-52) becomes. This regime is commonly known as the near Bragg region and $|\psi_0|^2 + |\psi_{\pm 1}|^2 \neq \psi_{\text{inc}}^2$ due to the generation of higher orders. In order to establish the Bragg region more precisely, the so-called Klein-Cook parameter Q has been defined

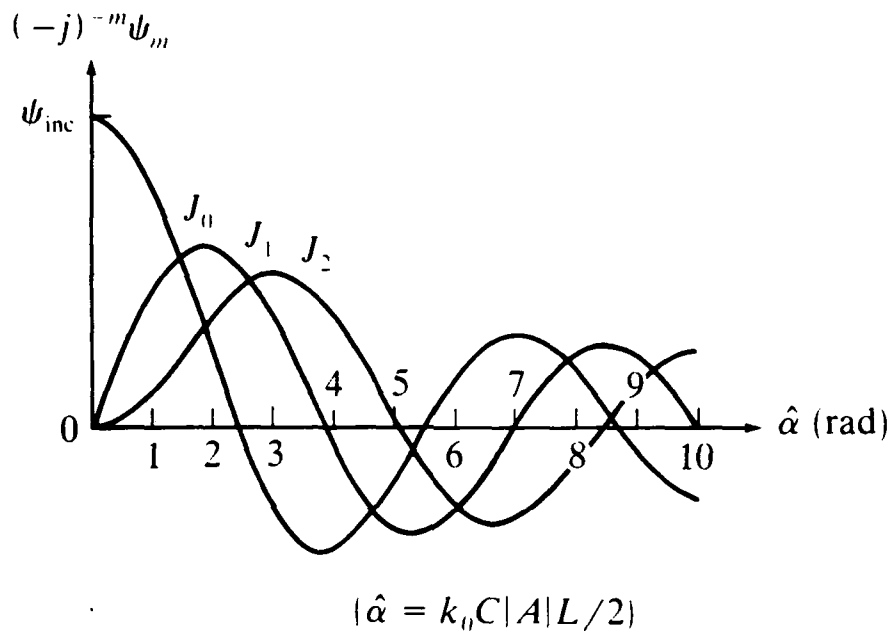
$$Q = (K^2/k_0)L, \quad (6.1-53)$$

and the amount of first order diffracted light is plotted as a function of Q at $\hat{\alpha} = \pi$. The Bragg region is then defined arbitrarily by the condition that $|\psi_{\pm 1}|^2 > 0.9\psi_{\text{inc}}^2$ (i.e., the diffraction efficiency for the first order light is greater than 90%), which has been shown to translate to $Q = (K^2/k_0)L > 7$. For $Q \rightarrow \infty$, $|\psi_{\pm 1}|^2 \rightarrow \psi_{\text{inc}}^2$ as expected.

6.1.3 Some Applications

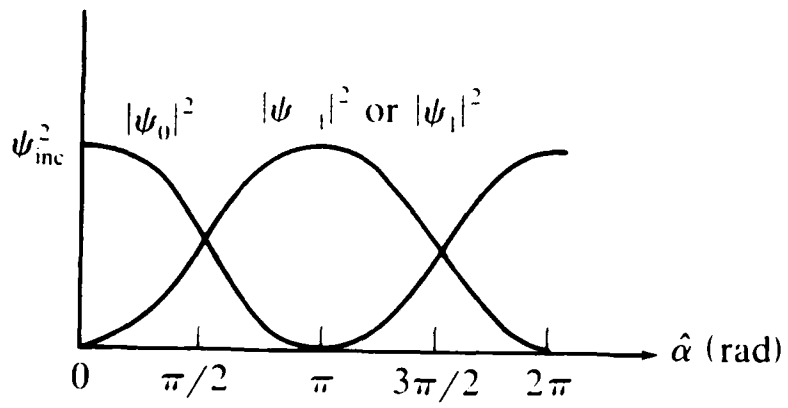
a) Intensity modulation of laser beam

A diagram of an intensity modulation system is shown in Fig. 6.9. The acousto-optic modulator is operated in the Raman-Nath region and only the zeroth-order



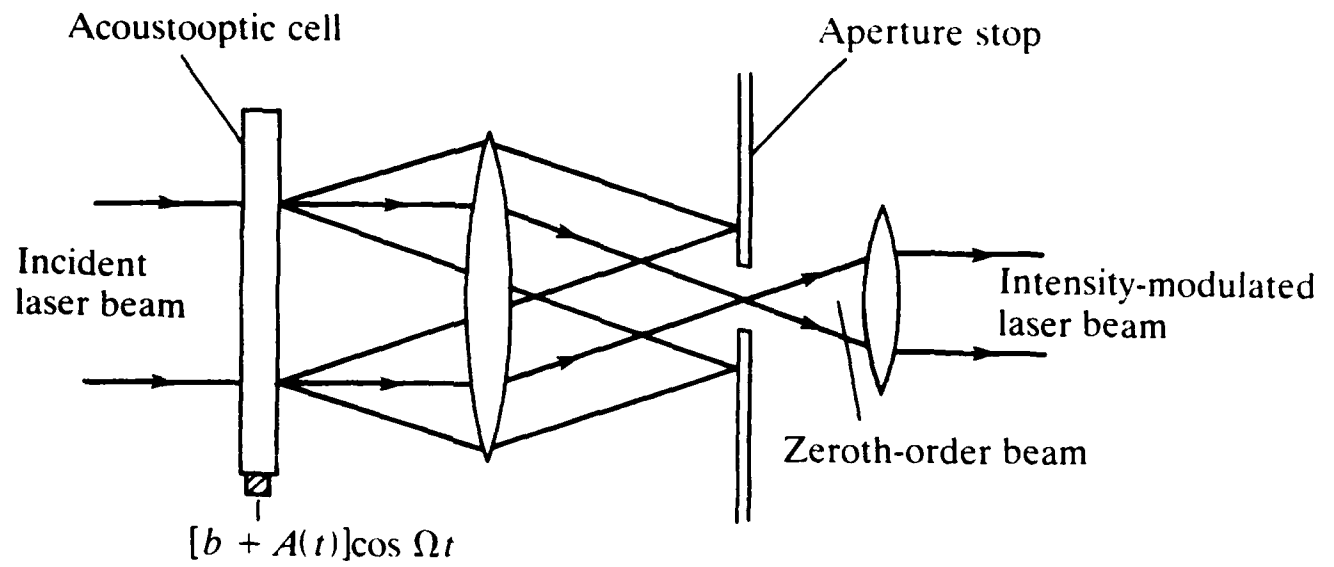
(a)

Figure 8 (a) Amplitude of diffracted orders in Raman Nath regime



(b)

Figure 8(b): Intensity of diffracted orders in Bragg regime



(a)

Figure 9: (a) An acousto-optic intensity modulation system

diffracted beam is allowed to pass through the aperture stop. With reference to Fig. 9b, linear operation may be achieved with a bias voltage b corresponding to around 1.3 radian peak phase shift of the light. Fig. 9b illustrates the relationship between the modulating signal $A(t)$ and the intensity modulated output of the laser beam. Although in Fig. 9a, the zeroth-order diffracted beam is used, it is clear that any diffracted order may be used in principle. In that case the aperture stop should be positioned at that particular beam used to achieve the modulation. Also, it should be clear that intensity modulation could be achieved similarly if the acousto-optic modulator is operated in the Bragg region.

b) Light beam deflector/spectrum analyzer

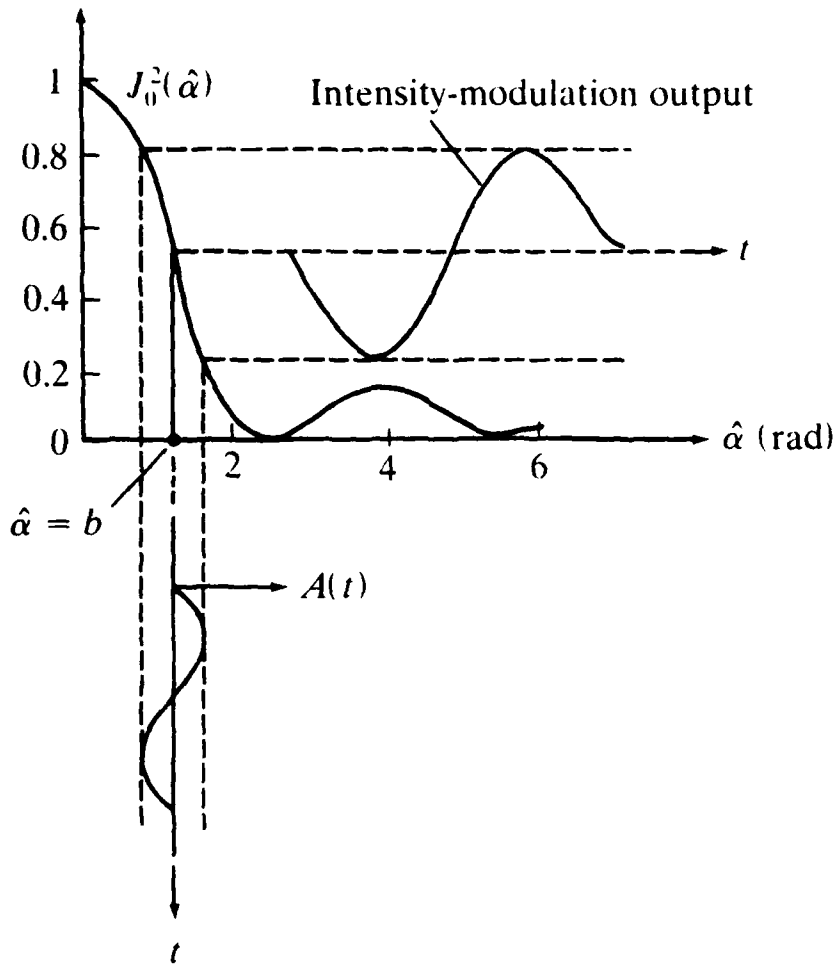
In contrast to intensity modulation where the amplitude of the modulating signal is varied, the frequency of the modulating signal is changed for applications in light deflection. Fig. 10 shows an optical beam deflector, where the acousto-optic modulator is operated in the Bragg region. The angle between the 1st-diffracted beam and the 0-th diffracted beam is defined as the deflection angle ϕ_d . The change in the deflection angle $\delta\phi_d$ upon a change $\delta\Omega$ of the sound frequency is given by

$$\begin{aligned}\delta\phi_d &= \delta(2\phi_B) \\ &= 2\pi \frac{\lambda_0}{V_s} \delta\Omega.\end{aligned}\tag{6.1-54}$$

The number of resolvable angles N in such a device is determined by the ratio of the range of deflection angles $\delta\phi_d$ to the angular spread of the scanning light beam. The angular spread of a beam of width D is of the order of λ_0/D , which follows from standard diffraction theory (see Chapter 3). Hence,

$$N = \frac{\delta\phi_d}{\lambda_0/D} = \tau \frac{\delta\Omega}{2\pi},\tag{6.1-55}$$

where $\tau = D/V_s$ is the transit time of the sound through the light beam. Note that improvement in resolution can be achieved by expanding the lateral width of the light beam traversing the Bragg cell. Since the relation between the deflection angle and the frequency sweep is linear, a simple mechanism for high speed laser beam scanning may be



(b)

Figure 9: (b) Relationship between modulating signal and output

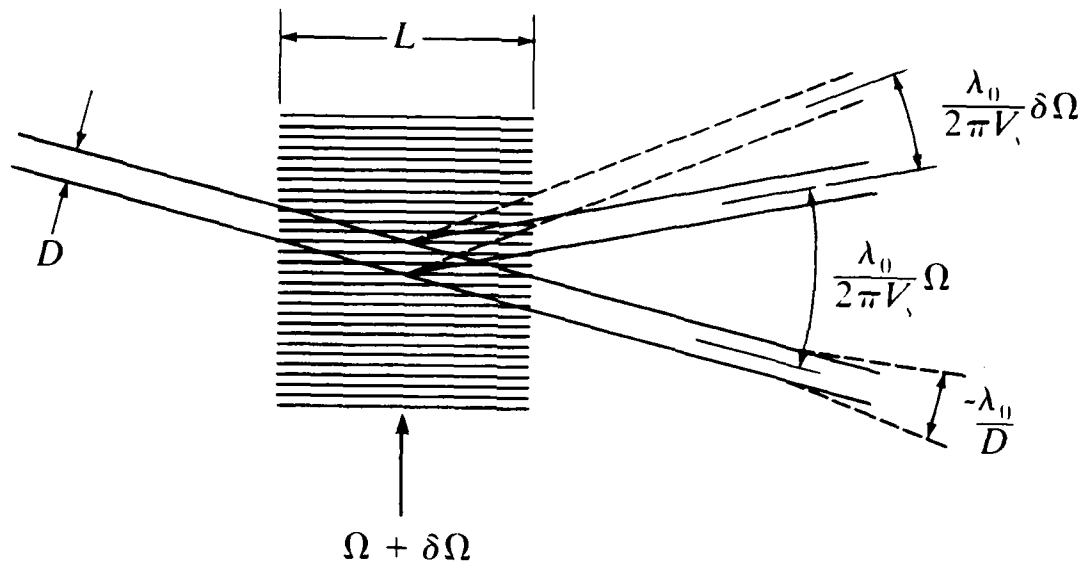


Figure 10: An acousto-optic light beam deflector

made possible through the acousto-optic effect because no moving mechanical parts are involved with this kind of scanning mechanism.

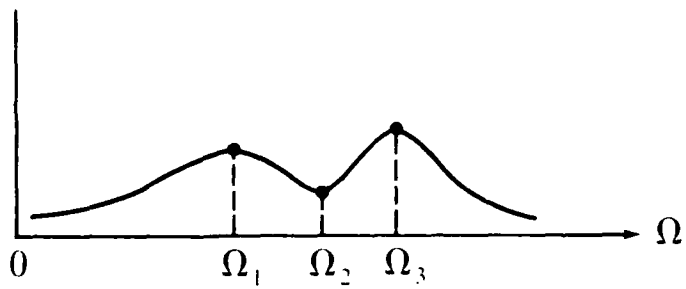
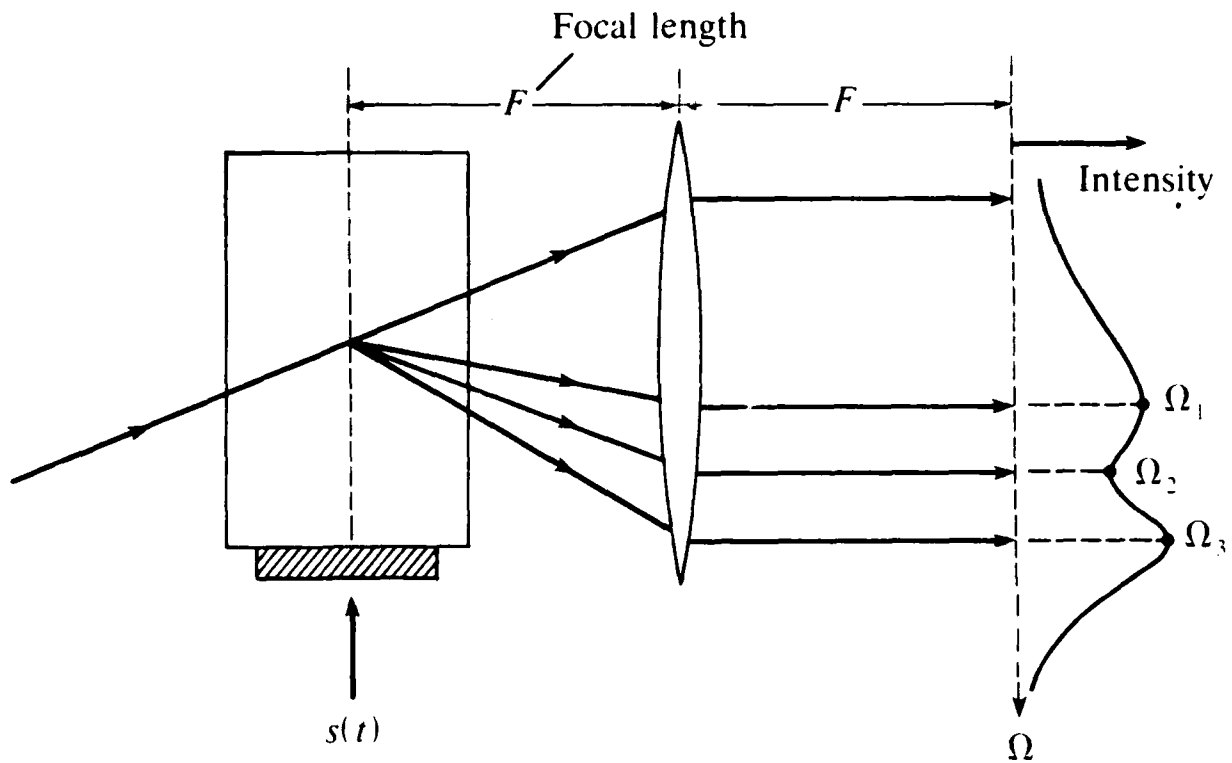
Instead of having a single frequency fed into the sound cell, it can be addressed simultaneously by a spectrum of frequencies. The Bragg cell diffracts light beams into angles controlled by the spectrum of acoustic frequencies as each frequency generates a beam at a specific diffracted angle. Since the acoustic spectrum is identical to the frequency spectrum of the electrical signal being fed to the cell, the device essentially acts as a spectrum analyzer. Fig. 11 depicts a convenient way to display the frequency content of the electrical signal $s(t)$. Note that frequency resolution of the analyzer is determined by N .

c) Demodulation of frequency-modulated (FM) signals.

From the preceding discussion, we recognize the Bragg cell's frequency-selecting capability. Here we discuss how to make use of this to demodulate FM signals. As seen from fig. 12 the Bragg cell diffracts light into angles ϕ_{di} controlled by the spectrum of carrier frequencies Ω_{oi} , where $i = 1, 2, \text{etc.}$ and each carrier has been frequency-modulated. For the i th FM station, the signal's instantaneous frequency can be represented as $\Omega_i(t) = \Omega_{oi} + \Delta\Omega_i(t)$ which is the sum of a fixed carrier frequency Ω_{oi} and a time-varying frequency difference $\Delta\Omega_i(t)$, the latter being proportional to the amplitude of the modulating signal. As a usual practice, the FM variation $\Delta\Omega_i(t)$ is small compared to the carrier Ω_{oi} . Using (6.1-54), the i th FM station is beamed, on the average, in a direction *relative* to the incident beam given by

$$\phi_{di} = \lambda_0 \Omega_{oi} / 2\pi V_s \quad (6.1-56)$$

This is illustrated in fig. 12. For each FM carrier, there will now be an independently diffracted light beam in a direction determined by the carrier frequency. For clarity, only a few of the diffracted light beams are shown. The principle of the receiver is that the actual instantaneous angle of deflection deviates slightly from the above angle due to the inclusion of $\Delta\Omega_i(t)$ which causes a "wobble" $\Delta\phi_{di}(t)$ in the deflected beam. In particular,



Frequency content of $s(t)$

Figure 11: An acoustooptic spectrum analyzer

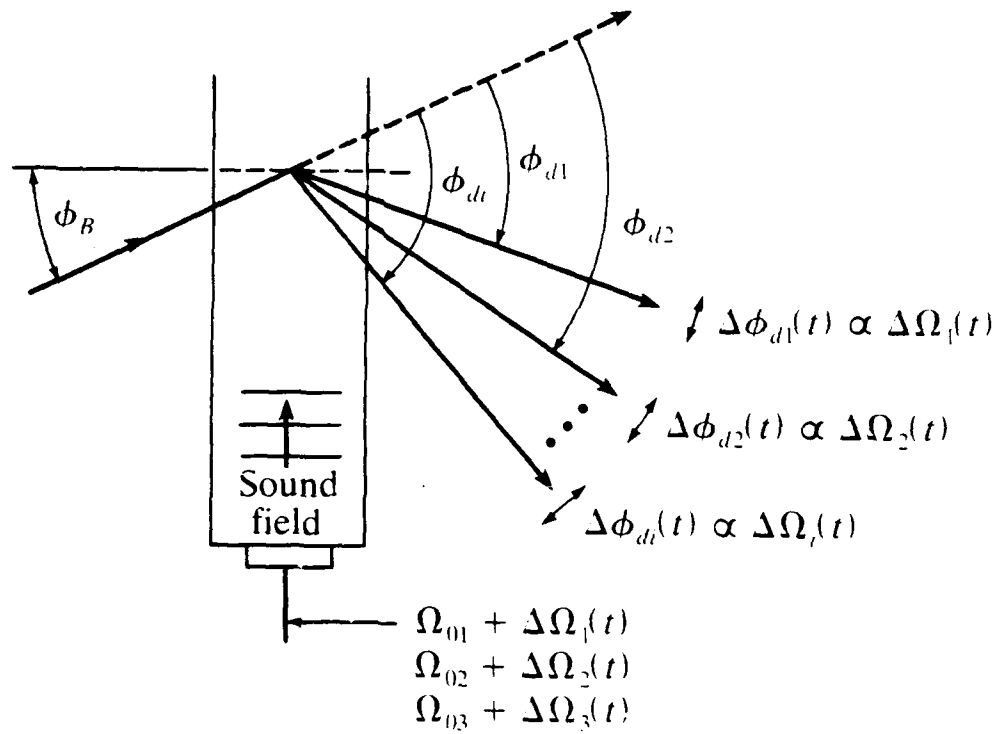


Figure 12: Nominal directions of diffracted beams due to FM sound inputs

we find, with (6.1-54),

$$\Delta\phi_{di}(t) = (\lambda_0/2\pi V_s)\Delta\Omega_i(t). \quad (6.1-57)$$

Since, in FM, the frequency variation $\Delta\Omega_i(t)$ is proportional to the amplitude of the audio signal, the variation in the deflected angle $\Delta\phi_{di}(t)$ is likewise proportional to the modulating signal. By placing a knife-edge screen in front of a photodiode positioned along the direction of ϕ_{di} , the amount of light reaching the photodiode, to first order, varies linearly with the small wobble $\Delta\Omega_i(t)$ and hence will give a current proportional to $\Delta\Omega_i(t)$ [see (6.1-57)], i.e., proportional to the amplitude of the modulating signal. In fact, by placing an array of knife-edge screened detector, we can monitor all the FM stations simultaneously. This knife-edge technique has been used previously for surface acoustic wave detection) (see, for example, Whitman and Korpel (1969)).



**MISSION
OF
ROME LABORATORY**

Rome Laboratory plans and executes an interdisciplinary program in research, development, test, and technology transition in support of Air Force Command, Control, Communications and Intelligence (C³I) activities for all Air Force platforms. It also executes selected acquisition programs in several areas of expertise. Technical and engineering support within areas of competence is provided to ESD Program Offices (POs) and other ESD elements to perform effective acquisition of C³I systems. In addition, Rome Laboratory's technology supports other AFSC Product Divisions, the Air Force user community, and other DOD and non-DOD agencies. Rome Laboratory maintains technical competence and research programs in areas including, but not limited to, communications, command and control, battle management, intelligence information processing, computational sciences and software producibility, wide area surveillance/sensors, signal processing, solid state sciences, photonics, electromagnetic technology, superconductivity, and electronic reliability/maintainability and testability.